Findings Report

Gondola for High Altitude Planetary Science
Science Instrument Definition Team

Date of Completion: September 28, 2016

Members:

Aslam, Shahid
Chanover, Nancy J. (Chair)
DiSanti, Michael A.
Hibbitts, Charles A.
Honniball, Casey
Paganini, Lucas (Co-Chair)
Parker, Alex
Skrutskie, Michael
Young, Eliot F.

Table of Contents

Executive Summary
2. Balloons for Planetary Science
3. A New Frontier with GHAPS
    3.1. Comparison with Other Assets
    3.2. GHAPS Optical Telescope Assembly
4. Considerations Unique to Balloon Platforms
    4.1. The Stratospheric Environment
    4.2. Thermal Considerations
    4.3. General Instrument Classes
5. Potential Science Drivers
    Optical / UV Spectral Region
        5.1.1 Kuiper Belt Object, Near-Earth Object, and Asteroid Binaries
        5.1.2 Venus cloud top characterization
        5.1.3 Cloud tracking on ice and gas giants
        5.1.4 Asteroid space weathering and resurfacing
        5.1.5 SO2 and Volcanism on Io and Venus
    Near IR through Mid-Wave IR
        5.2.1 Jupiter's Aurorae
        5.2.2 Variability of Lunar Water
        5.2.3 Organics and Volatiles on Asteroids
        5.2.4. Volatiles in Comets
            5.2.4.1 Carbon dioxide (CO2)
            5.2.4.2 Methane (CH4) and carbon monoxide (CO)
            5.2.4.3 Water (H2O)
        5.2.5 Water in plumes of icy ocean worlds
    Thermal IR (TIR)
        5.3.1 Heterogeneity of the Lunar Mantle
        5.3.2 Volatiles on Mercury
General Purpose vs. Spectrally Optimized Flights
    Image Scale
    System Emissivity and Thermal Infrared Sensitivity
    Instrument Cryogenic and Power Requirements
    References
Appendix 1: Master list of instrument requirements for science cases in Section 5.
Appendix 2: UV-VIS SNR Estimation
    Example SNR Calculation
        Calculating Source Counts
        Calculating Noise Terms
    Advantages of a Balloon Platform in the UV/Optical
        High Acuity Imaging
        Photometric Stability and Low Sky Background
Appendix 3: Calculating the Nominal Sensitivity of a Hypothetical GHAPS IR Science Instrument
    Sensitivity to line and continuum flux

Magnitude limits
Appendix 4: Acronym List

1. Executive Summary

NASA is currently developing the Gondola for High-Altitude Planetary Science (GHAPS), which will be an observing asset hosted on stratospheric balloon missions. It will be a shared and competed community resource with a suite of facility instruments that observers can propose to use for their respective scientific investigations (Fig. 1).

NASA convened the GHAPS Science Instrument Definition Team (SIDT) in May 2016 and tasked it to help define instrument priorities for GHAPS. The SIDT reviewed the current status of the GHAPS optical telescope assembly (OTA), lessons learned from previous planetary science balloon flights, existing instrument technologies, and the most recent Planetary Science Decadal Survey (NRC 2011). The SIDT was charged with defining the scope of science investigations, and based on this defining science requirements and presenting instrument concepts for GHAPS, identifying potential instrument types according to science priorities that address Planetary Science Decadal Survey questions. The findings contained in this document are the results of these efforts on behalf of the SIDT.

GHAPS will complement ground-based telescopes, the Stratospheric Observatory for Infrared Astronomy (SOFIA) and the Hubble Space Telescope (HST) by virtue of its low-cost access to near space with repeated flights each lasting up to 100 days. **Several key advantages of GHAPS include:**

- access to wavelengths that are inaccessible from ground-based and airborne facilities
- temporal coverage
- high spatial resolution at short wavelengths and high spectral resolution spanning from UV to IR wavelengths

The key findings of the SIDT concerning the GHAPS science instrument requirements are as follows:

- There are science drivers for a wavelength coverage spanning 0.20 – 30 μm, including both imaging and spectroscopic capabilities at most wavelengths.
- A fine guiding capability (jitter < 30 milliarcsec RMS) is critical for a number of measurements, particularly at UV and visible wavelengths. The pointing system to be implemented with GHAPS may need to be augmented with a fine guidance capability in the individual instruments.
- The capability to track objects at non-sidereal rates is critical for many solar system targets.
- The ability to conduct investigations requiring short exposures (10s of milliseconds) with a high duty cycle (~ 50%) over a time span of several hours, to those needing longer exposures (seconds to minutes) with lower duty cycle (e.g., up to days), encompassing the wide range of temporal variability that can be explored from a balloon-borne platform.

- IR observations benefit from OTA temperature below ~ 230 K.

The imaging applications examined by the GHAPS SIDT involved:

- a field of view (FOV) of one to several (~ 3) arcminutes.
- high image acuity over all wavelengths (assumed to be diffraction limited).
- a judiciously selected combination of narrowband and broadband filters.

The spectroscopic applications examined by the GHAPS SIDT involved:

- spectral resolutions ($R = \lambda/d\lambda$) ranging from low (50 in LWIR) to medium (1000 in UV) to high (greater than 5,000 in IR).
- a range of desirable instrument modalities, including long-slit (>10") spectroscopy for both UV and IR applications to study extended objects, and two-dimensional spectroscopy (e.g. using an integral field unit or hyperspectral imaging) for spectroscopic mapping of spatially resolved targets.

These requirements are noted for the individual science cases in Tables 4-15, and they are combined into a single master table (Table A.1) in Appendix 1. In addition, this report contains several Appendices that discuss specific issues that may be relevant to instrument proposers, such as examples of signal-to-noise calculations or justification for a minimum field of view.

Not all decadal-class science questions will be amenable to study from the stratospheric GHAPS telescope, but certain questions are well-suited to the advantages afforded by long-duration balloon missions in the upper stratosphere. The principal charge for instrument proposers will be to devise instruments that take advantage of the balloon environment while also overcoming associated challenges (such as delivering ultra-stable pointing in the visible or mitigating thermal variations within the OTA) while providing measurement capabilities that meet the needs of the planetary community.

We present the background of balloon missions for planetary science in §2. Details of the GHAPS project are given in §3, while §4 presents the unique aspects of the high-altitude environment. This report considers sixteen science cases covering a broad range of planetary science enabled by a stratospheric telescope (§5). Examples include investigating volatiles on Mercury, asteroids, and the Moon, the detection and characterization of faint KBO companions, tracking of clouds on ice giants, detections of plumes in icy worlds, and spectroscopy of comets. While not an exhaustive list of science topics, these examples are intended to help define instruments that can address such studies and that will be broadly useful to the planetary science community. A set of instrument requirements was identified for each of the science cases discussed in §5. These include requirements on the FOV size, wavelength range, spectral resolution, spatial resolution, operational mode (e.g. imaging, slit spectroscopy, etc.), pointing and tracking, sampling cadence, signal-to-noise ratio (SNR), and subsystem temperature. A comparison between general purpose and spectrally optimized flights of GHAPS is given in §6.

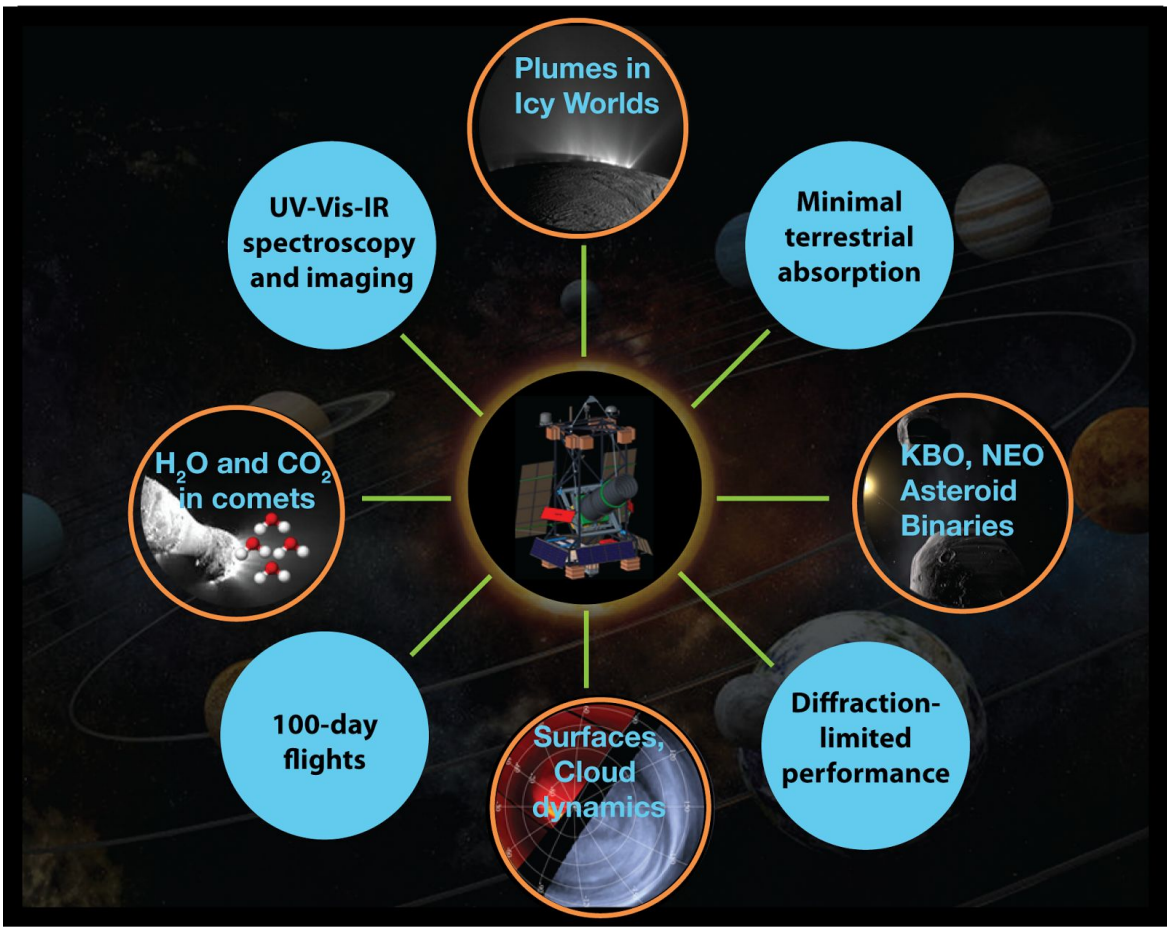

Figure 1. Schematic showing example science cases that GHAPS can address, along with the principal advantages offered by a balloon-borne observatory for planetary science.

2. Balloons for Planetary Science

NASA's balloon program has played a fundamental role in scientific discoveries, technology development, and the training of new generations of scientists and engineers since the 1970's. Balloon-borne investigations have led to fundamental measurements of cosmic ray antiprotons, the polarization of the cosmic microwave background radiation, the heating of the solar chromosphere, and chlorofluorocarbons in the Earth's stratosphere. With improved fine guiding, pointing capabilities, and the possibility of longer duration flights using super-pressure and zero-pressure balloons, planetary science is expected to be the next realm in which balloon-borne investigations can make significant contributions to decadal-level science questions.

Conventional (i.e., zero-pressure) balloon flights typically last no more than a few days, although if launched during summer from Antarctica, can persist for up to a few weeks. There is a direct tradeoff between balloon size, maximum allowed weight for the payload, and float altitude (Fig. 2). NASA is currently in the demonstration phase of missions transported by superpressure balloons, allowing the support of payloads of up to 1800-2700 kg (4000-6000 lb) at altitudes of 34 km (110,000 ft) and extending for up to 100 days.

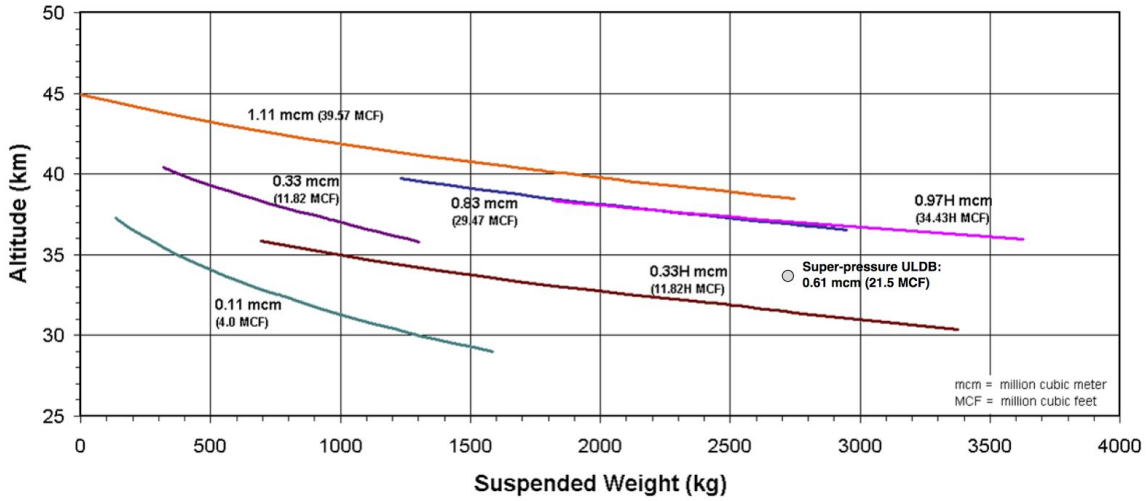

Figure 2. Load/altitude curves from NASA's Columbia Scientific Balloon Facility (http://www.csbf.nasa.gov/balloons.html) with a data point added for prospective super-pressure balloons.

A balloon-borne platform for planetary science measurements represents a relatively new class of assets for achieving decadal class science. Recent advances in super pressure balloons, which allow for longer duration flights, as well as improved pointing capabilities have made balloon-borne platforms an attractive, lower-cost alternative to planetary space flight projects. In January 2012 NASA convened a workshop entitled *Exploring the Planetary Science Achievable from a Balloon-Based Observatory*, at which members of the planetary science community identified a number of science cases and mission concepts for balloon platforms with traceability to the planetary decadal survey (NRC 2011).

Following this workshop, in February 2013, NASA directed a team of investigators from Glenn Research Center, the Johns Hopkins University Applied Physics Laboratory, and the Southwest Research Institute to develop a balloon flight, Balloon Rapid Response for ISON (BRRISON), for conducting observations of comet D/2012 S1 (ISON) that had a close approach to Earth (~ 64 million km) in early November 2013. This was a fast paced, high risk mission that, once developed, would be available to conduct new missions potentially every year. Truly a new paradigm for NASA scientific ballooning, BRRISON presented the possibility of achieving cheap, focused, high value NASA planetary mission science. Although an anomaly prevented the deployment of the telescope and no science results were obtained for BRRISON, the successful launch,

operation, and recovery were a technical demonstration of the potential of NASA scientific ballooning to conduct high-value planetary science 'decadal-level' measurements.

The BRRISON experience added tremendous insights for the development of the Balloon Observation Platform for Planetary Science (BOPPS) mission, a follow-up flight with similar concept, and the first with a well defined science objective (Cheng et al., 2016). It launched from Ft. Sumner, NM on September 25, 2014 and ascended to a float altitude of 39 km. Featuring a UV-Vis and multispectral IR imager, BOPPS targeted the quantification of water and carbon dioxide outgassing from comets C/2013 A1 (Siding Spring) and C/2014 E2 (Jacques), and measurement of the 3 μm water absorption band in the surface material on Ceres (Cheng et al. 2014).

In October 2014 NASA's Balloon Program Office launched the Observatory for Planetary Investigations from the Stratosphere (OPIS), which was an internal effort from Goddard Space Flight Center to demonstrate the capability of the Wallops ArcSecond Pointing (WASP) system. The OPIS flight demonstrated the capabilities of the WASP system to deliver sub-arcsecond pointing control, with residual RMS < 0.5" and a short-term pointing stability that can enable observations of extended solar system targets.

Detailed summaries of the BRRISON, BOPPS, and OPIS demonstration flights are given in Dankanich et al. (2016). These balloon flights achieved several key accomplishments that paved the way for the development of GHAPS, notably the demonstration of technologies such as a fine steering mirror and sub-arcsecond pointing as well as unique science results such as the first direct measurement of water production rate in a comet from balloon altitude (Cheng et al. 2016). Planetary science flights will require more accurate pointing and guiding than typical astrophysics investigations. However, this is not unprecedented; for example, the SUNRISE experiment required precise target acquisition and tracking to study magneto-convective processes on the Sun (see e.g. Barthol et al. 2011).

3. A New Frontier with GHAPS

The GHAPS concept is intended to be a reusable asset for planetary science observations from a balloon platform. GHAPS is designed for a minimum of five flights, each up to 100 days (or perhaps more) in duration, with minimal maintenance between flights. The GHAPS system capability is expected to evolve over time based on science demands. A competitive process will be used to select investigators based primarily on proposed science. The strengths of GHAPS observations will be in the 300 nm to 5 μm wavelength region covering UV, visible, and near-mid IR, with the potential for extending to longer wavelengths for sufficiently bright targets. GHAPS is being designed to support a 1-meter aperture narrow field-of-view telescope with sub-arcsecond pointing accuracy. Utilizing NASA's stratospheric balloon capabilities, GHAPS will fly at altitudes between 31 – 40 km (100,000 – 130,000 ft) where observations can be made above more than 99.5% of Earth's atmosphere. The overall system characteristics and environmental performance specifications of GHAPS are given in Table 1.

Table 1. GHAPS Overall System Characteristics and Environmental Performance Specifications

Item	Value or Range	Rationale/Comment
Operating Altitude	31 – 40 km	GHAPS shall operate at flight altitudes between 31 and 40 km (100K – 130K ft)
Operating Altitude Duration	Up to 100 days	
Environment Temperature at Float Altitude	From -50 ºC to 20 ºC	At float altitude of 37 km
Operating Altitude Pressure	~ 4 torr	At float altitude of 37 km
Ascent Temperatures	Start : 20 ºC Lowest: -70 ºC Final minimum: -40 ºC	Ground morning launch preparation Tropopause (Lowest temp. encountered for up to 60 minutes) Stratosphere (at float altitude of 34 km)
Ascent Pressure Change	760 to 4 torr	
Ascent Time	2 to 3 hours	240 m/min (typical)
Descent Temperatures	Similar to ascent	Similar to ascent
Shipping and handling Temp Limits Before and After Launch	-90 ºC to 50 ºC	Summertime temperatures in Ft Sumner, NM may reach 50 °C a few inches above the launch pad, and temperatures at the gondola's height several feet above the pad may exceed 40 °C. Temperatures in Antarctica can range from 5 °C to -15 °C during the campaign (October-January). Note: -90 ºC temperature could occur in Antarctica if OTA could not be promptly recovered and had to winter over on ice.
Balloon and Payload System Deployment G loads	0.5 to 2 g	Events due to balloon spool release, and launch vehicle payload/balloon release.
Payload System Ascent G loads	0.5 g	Typically due to wind loads
Payload System Descent G loads	2-5 g	Due to parachute opening

Payload System Landing G loads	10 g	Maximum allowable design stopping load
Recovery and Ground Transport G loads	5 to 7 g	Open trailers, and the road trip from the landing site back to the launch facilities
Elevation angle (operating)	0° to +65°	
Elevation angle (survival)	-90° to +90°	

3.1. Comparison with Other Assets

With an abundance of decadal-level planetary science questions achievable from a balloon-borne platform and the existing technological capabilities to support these investigations, we can examine the relative advantages of balloons versus other observing platforms. Metrics that can be used to compare various observational assets include time allocation and availability, the degree to which the observations can be made (or are required to be made) from above most of the Earth's atmosphere, spatial resolution, pointing accuracy, observing efficiency, telescope aperture, and average cost per observational campaign. A comprehensive trade study of these various criteria is beyond the scope of this report (see Dankanich et al. (2016) for a detailed discussion). Figure 3 shows a general decision tree for determining the suitability of a balloon-borne platform for certain scientific investigations, along with two specific examples to demonstrate that balloons offer a unique and valuable observational capability. Figure 4 is a schematic depicting the multitude of capabilities afforded by GHAPS.

We note that there are several key drivers for balloon-borne investigations, namely a) access to wavelengths that are inaccessible with ground-based telescopes, especially in key areas of investigation related to the study of water and carbon dioxide at IR wavelengths and other molecules in the UV, b) the ability to achieve temporal coverage that is not obtainable elsewhere (either due to the oversubscription of space-based assets like HST or due to the diurnal cycle imposed on all Earth-based observations), and c) the ability to achieve high spatial resolution at short wavelengths.

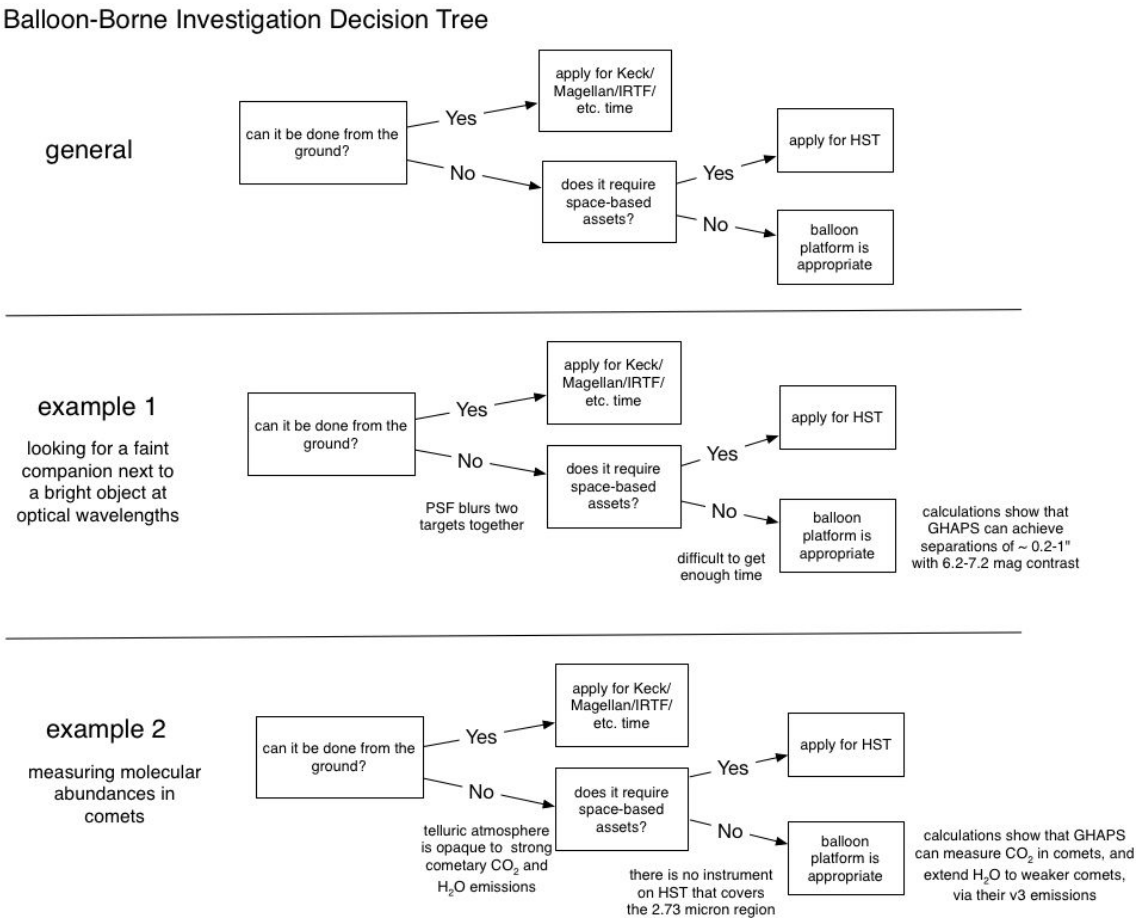

Figure 3. A notional decision tree showing the thought process a potential PI may use when deciding which asset to propose to, and whether a balloon-borne platform is appropriate for a given planetary science measurement objective. A generic decision tree is shown in the top panel while the application of that tree to two specific examples (discussed further in Sections 5.1.1 and 5.2.4, respectively) is shown in the middle and bottom panels.

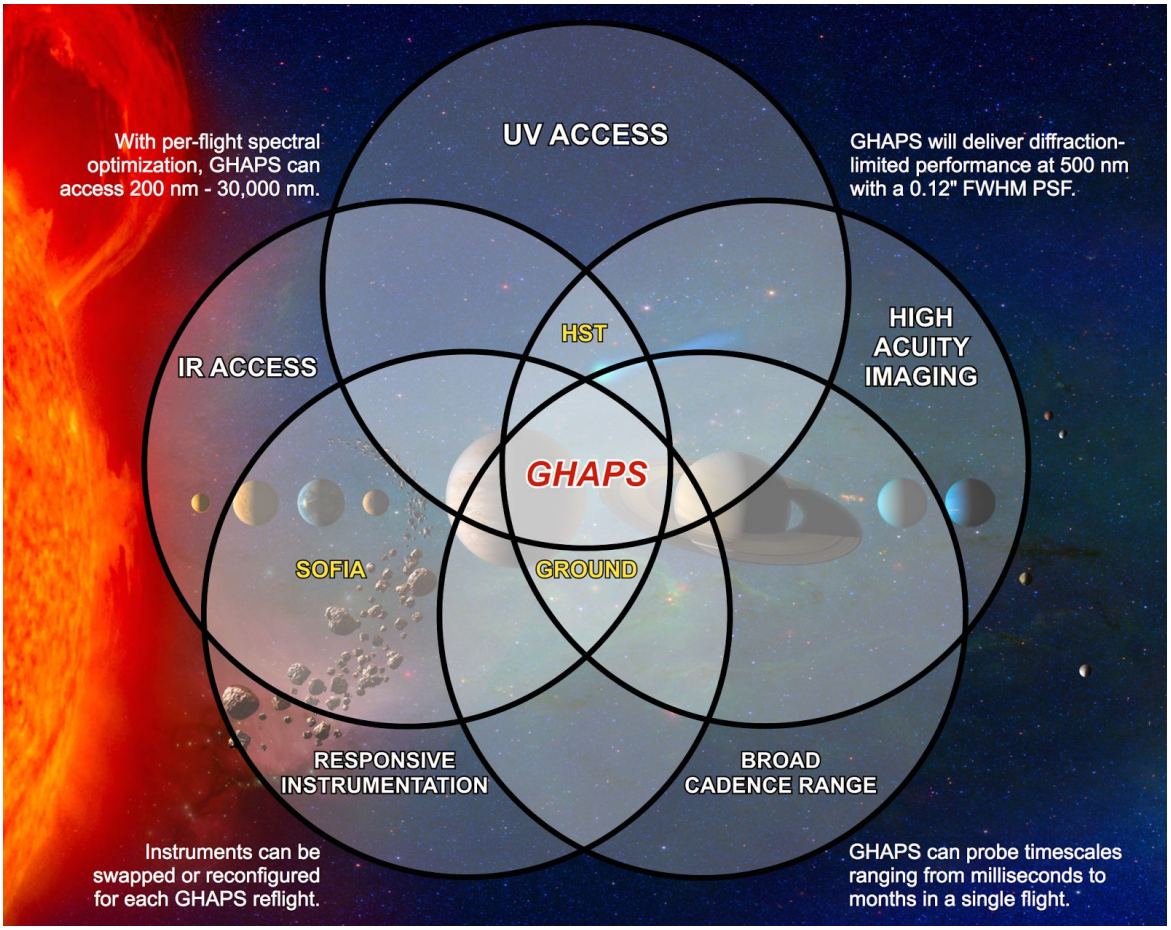

Figure 4. Schematic depicting the unique capabilities afforded by GHAPS as well as the synergies between GHAPS and other assets used for solar system observations.

3.2. GHAPS Optical Telescope Assembly

In order to explore the planetary science questions that can be addressed with GHAPS and identify a set of instrument requirements, the GHAPS SIDT made a number of assumptions about the GHAPS Optical Telescope Assembly (OTA). These were based on information provided to the SIDT by the GHAPS Project. Instrument developers are advised to verify that they are using the most up-to-date information about GHAPS, as some of the design features are not fixed at the time of this writing.

The GHAPS OTA is a Richey-Crétien Cassegrain telescope with a 1-m aperture and a focal length near 14 m. It will support UV to IR science instruments with a 3-arcmin FOV. The focal length is derived from the angular size of the PSF at the visible and IR operating wavelengths (the PSF width is defined here as the wavelength-dependent diffraction limit: 1.22 λ/D). Thus, the selected GHAPS focal length of 14 m is approximately the geometric mean of desired focal lengths at visible and IR wavelengths that will deliver the diffraction-limited PSF. It is expected that through their optical design visible instruments will have to extend the OTA focal length by a factor of 3, while IR

instruments will reduce the focal length by a factor of 3. The optical performance specifications of GHAPS are given in Table 2.

The pointing requirements also scale with wavelength: it makes sense to stabilize the telescope such that root-mean-square (RMS) motions are less than the PSF width. At least two previous balloon missions (Sunrise and BOPPS) achieved focal plane stabilities near 0.05". Both used a coarse pointing system to keep the telescope within a few arcseconds of the target, then a fine steering system to further align the focal plane to the sub-arcsecond level. GHAPS is slated to use WASP for coarse alignment. The 3σ stability of WASP is expected to be less than 1.5". Instruments are expected to derive their own pointing errors and affect fine-scale pointing corrections.

Table 2. OTA Optical Performance Specifications

Item	Value or Range
Aperture	1 meter
Focal length	14 meters
Telescope focus axial position	0.5 meters behind primary mirror vertex
Wavefront error (WFE)	$\leq$ 26 nm (RMS) at 500 nm
Field of View Dia. NUV-Visible-NIR	1 arc-min diameter
Field of View Dia. IR	≥ 3 arc-min diameter; diffraction limited over central 1 arc-min diameter
Wavelength range: NUV-Visible-NIR	0.30 - 1.0 μm[1]
Wavelength range: IR	2.5 - 5.0 μm[1]
Obscuration ratio	≤ 30% linear, < 15% areal
Stray light	< 1 x 10^{-12} point source normalized irradiance transmittance (PSNIT) for point source 40° off OTA line-of-sight
Mirror reflectivity	≥ 95% in NUV-Visible-NIR; ≥ 98% in IR from 3 to 5 μm
Mirror IR emissivity	≤ 2% emissivity in IR
Mirror coating durability & adhesion	Per MIL-C-48497A; withstand CO_2 'snow' cleaning

[1]The GHAPS OTA is optimized for diffraction-limited performance between 0.5 - 5.0 μm. However, with appropriate optical coatings the short wavelength end may be extended to 0.2 μm and the long wavelength end to 30 μm.

4. Considerations Unique to Balloon Platforms

4.1. The Stratospheric Environment

The high altitude of typical balloon flights provides an observational advantage over ground-based telescopes throughout the 1 to 5 μm region (and beyond) because of reduced telluric opacity and reduced downwelling radiance. At float altitudes, where the atmospheric pressure is about the same as on the surface of Mars (~5 mbar, or 3 – 8 torr), GHAPS will fly above 99.3 – 99.6% of the atmosphere for uniformly mixed gases, and also above virtually all atmospheric water vapor, with approximately 0.3 μm of precipitable water and a frost point near 180 K. Additionally, at altitudes of 30 – 35 km the thin atmosphere is sufficiently free of turbulence, with a Fried parameter (R_o) estimated to be several meters or more, compared to a few 10s of cm for the best ground based observatories. This means that a balloon-borne telescope can see as sharply as a comparable telescope in space (Ford et al. 2002).

For UV and visible wavelength observations, the most dramatic improvements in atmospheric transmission occurs in the 280 - 400 nm range. For example, at 300 nm, the transmission from 35 km (115,000 ft) altitude is about 80%, but less than 5% for observers on the ground or even on SOFIA.
Balloon-borne platforms are blocked from 240 - 280 nm, but a window opens up in the 200 - 230 nm range (Fig. 5). Note that this wavelength range requires special attention to mirror coatings and surface finish.

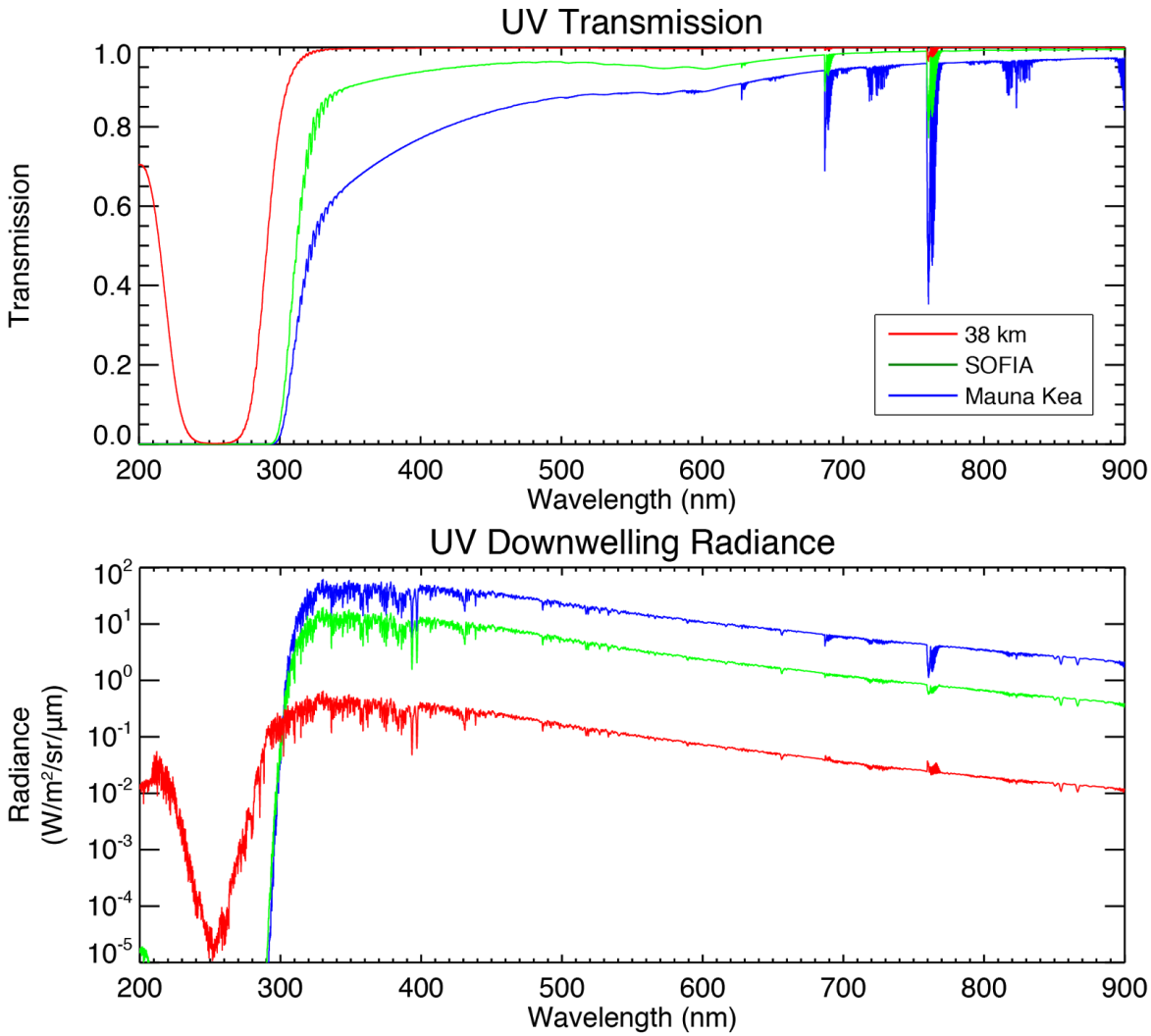

Figure 5. MODTRAN atmospheric modeling results showing the expected UV vertical transmittance through (top panel) and spectral radiance of (bottom panel) the terrestrial atmosphere from 4.2 km (blue), 13 km (green), and 35 km (red) for summer daytime continental conditions, showing the dramatic improvement in both at GHAPS altitude. At night, the radiance drops to near zero, except for airglow lines.

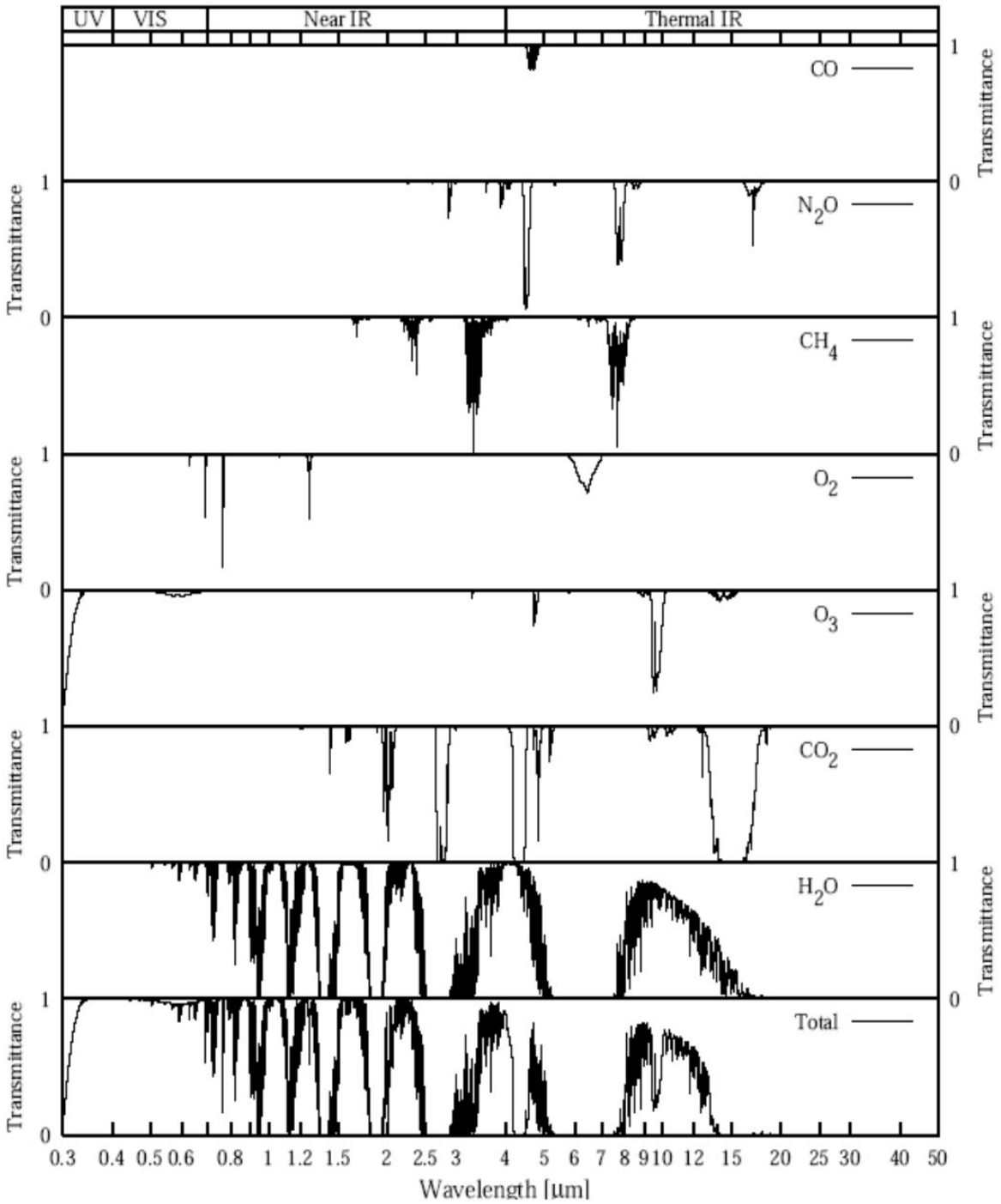

Figure 6. High resolution spectra of the main sources of atmospheric attenuation in Earth's atmosphere as seen from the ground.

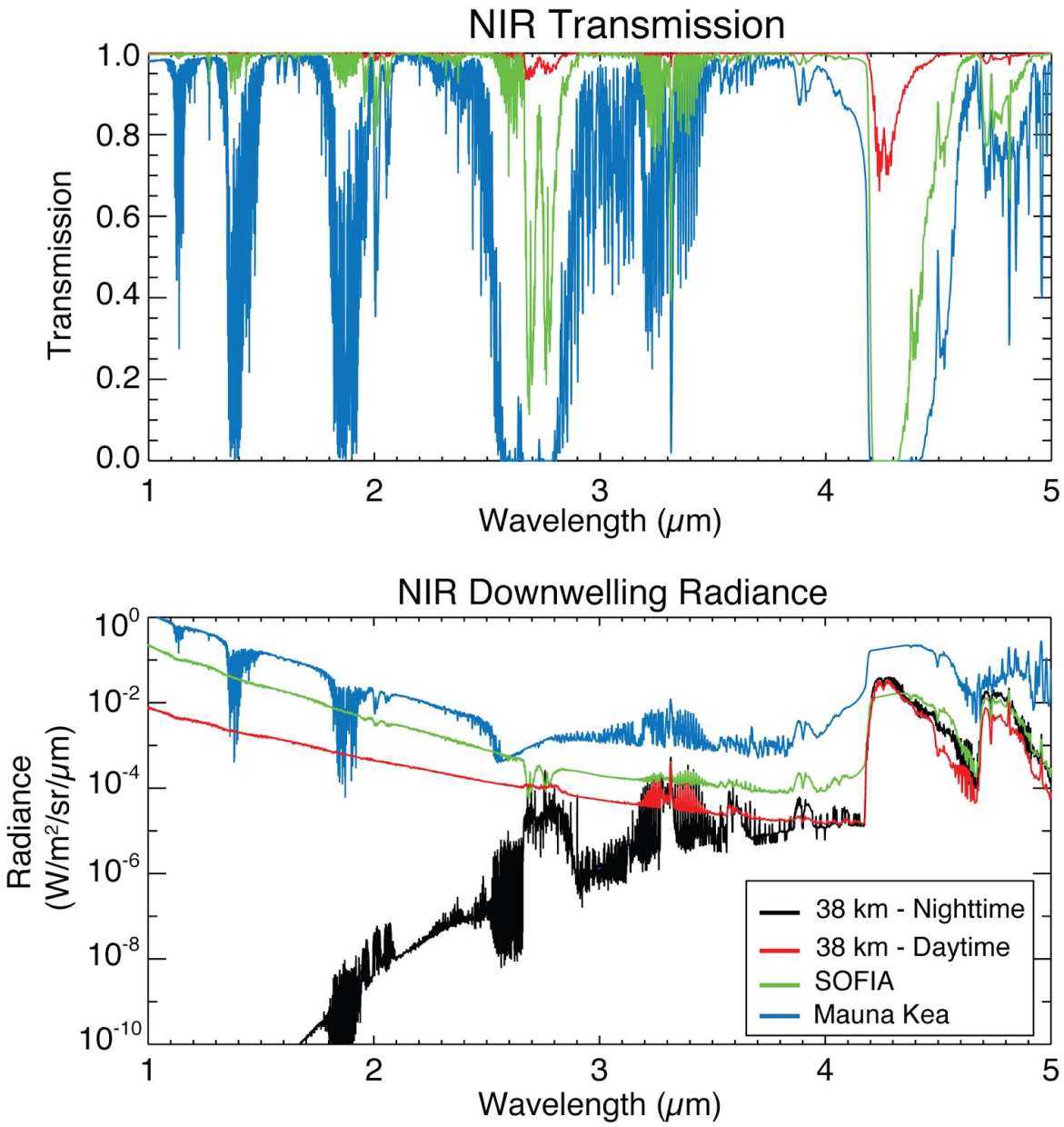

Figure 7. Atmospheric vertical transmission (top) and downwelling radiance (bottom) for altitudes corresponding to Mauna Kea (blue), SOFIA (green), and a balloon at 38 km (127,000 ft) (red) calculated at 1 cm^{-1} resolution for continental summer daytime conditions and a vertical perspective. At night, the lack of scattered sunlight results in the radiance decreasing at wavelengths shortward of 4 μm, to below 10^{-5} $W/m^2/sr/\mu m$ by 3 μm (black trace in bottom panel). The radiance of the modeled CO_2 and CO features near 4.3 and 4.6 μm are not expected to change significantly during nighttime. The larger nighttime radiance at the optically thick CO_2 and CO bands comes from assuming a somewhat lower altitude (30 km) and relatively high air mass (a viewing geometry of only 20° above the horizon). The nighttime downwelling curve lacks the contribution from the zenith airglow component, but we show it in Fig. 9 and consider it in our sensitivity calculations in Appendix 3.

In the infrared spectral region, the Earth's atmosphere is the main source of attenuation due primarily to absorption, producing a reduction in amplitude and intensity of light from celestial objects. The main sources of atmospheric attenuation are terrestrial water vapor, carbon dioxide, methane, ozone, nitrous oxide and carbon monoxide occurring below the tropopause (Fig. 6). If we consider an ideal noise-free system, terrestrial emission would set the lower limit for observational background noise at many IR wavelengths and telescope mirror temperature at the more transparent IR wavelengths. Therefore, noise estimates and strategic instrument design should aim for noise levels below (or as low as possible compared to) the thermal contribution from the sky. However, even in such an ideal case detector read noise could become substantial below 3 μm (in particular for nighttime observations; see the black trace in Fig. 7), based on current state-of-the-art specifications and detector technologies.

The atmospheric absorption and downwelling radiance is a function of altitude. For instance, compared to ground-based platforms, airborne facilities like the (retired) Kuiper Airborne Observatory (KAO) and SOFIA, at an altitude of ~13 km, experience less attenuation by being above approximately 99% of the total atmospheric water burden. For super-pressure and zero-pressure balloon observatories, at altitudes above 28 km (i.e. higher in the stratosphere), the atmosphere is virtually "transparent" in the H_2O bands, resulting in lower background noise and atmospheric transmittance approaching unity.

Infrared observations from the ground are largely limited to atmospheric windows; wavelengths between 5 and 8 μm, and beyond 14 μm are almost entirely inaccessible. However from balloon altitudes, the transmission is high throughout the infrared, even in the CO_2 v_2 band near 15 μm, allowing unique observations not possible from ground-based telescopes, and in some cases not available from existing or planned spacecraft platforms (Fig. 8). Compared to the telescope thermal emission, the path radiance is largely negligible, and is weak even in the core of the infrared ozone and CO_2 bands. In the low-transmittance and variable 20-μm window, GHAPS is far superior to any ground-based telescope because of the high transmission and low downwelling radiance.

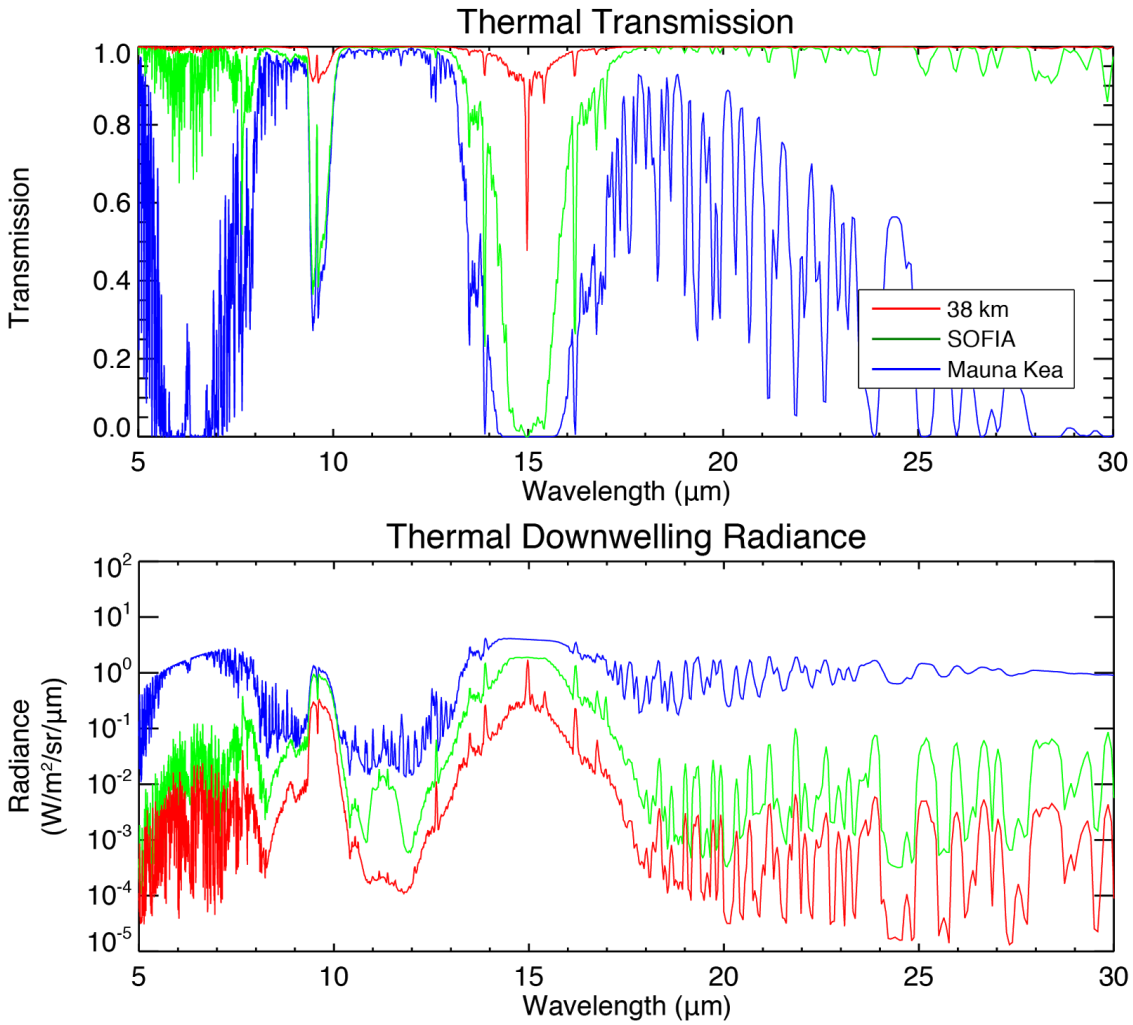

Figure 8. Thermal atmospheric vertical transmission (top) and downwelling radiance (bottom) for altitudes corresponding to Mauna Kea (blue), SOFIA (green), and a balloon at 38 km (red) calculated at 1 cm^{-1} resolution for continental summer daytime conditions. Panels are analogous to those in Figures 5 and 7 for shorter wavelengths.

Infrared observations from the ground are largely limited to atmospheric windows; wavelengths between 5 and 8 μm, and beyond 14 μm are almost entirely inaccessible. However from balloon altitudes, the transmission is high throughout the infrared, even in the CO_2 v_2 band near 15 μm, allowing unique observations not possible from ground-based telescopes.

The downwelling radiance from the atmosphere is a factor of several lower at balloon altitudes than at SOFIA altitudes (12 km), and orders of magnitudes less than Mauna Kea. Radiation from extended objects having temperatures above those of the stratosphere should dominate background levels. Denny et al. (2013) performed a study on the fundamental limits of thermal IR detection from 30-3000 microns. They compared three platforms: (1) the 25 m telescope at Cerro Chajnantor, Chile, (2) the 2.5 m telescope on board SOFIA flying at an altitude of 14 km with the optics at 230 K, and (3)

two variations of a high altitude balloon observatory at an altitude of 40 km, one a 2.2 m telescope operating at 2 K and 230 K, and the other a 10 m telescope operating at 230 K. For the balloon cases they concluded that downwelling radiance and ambient thermal emission were comparable, and also that the atmospheric background is an order of magnitude lower than for the best ground-based observatories. Thus for bright objects, the performance of a balloon telescope can be reasonably estimated to be limited by mirror temperature and emissivity. Clearly, for extended objects with emissivity near unity and surface temperatures above (or far above) the mirror temperature, the signal-to-noise is expected to be dominated by source signal, and not by emission from the atmosphere or mirror.

4.2. Thermal Considerations

As mentioned in § 2.1, GHAPS observations will sometimes be background limited, particularly in the mid-infrared, so the sensitivity of the payload instruments will need to exceed the scattered and self-emission background. The background is a combination of in-field atmosphere, airglow, zodiacal light, scattered thermal emission from the sunshield (baffle) and telescope, and near-field optics. Figure 9 shows the wavelength dependence of the expected effective background radiance of the GHAPS observatory (resulting from the OTA mirrors) compared to the emission from the Earth's atmosphere (including airglow). An optimal sensitivity is achieved when the atmospheric emission exceeds the total thermal emission from the telescope. Considering that telescope components emit as blackbodies, it is desirable for the primary and secondary mirrors to operate at relatively cold temperatures and to use coatings featuring low emissivities, which result in low thermal irradiation. The telescope spiders, baffles and struts, characterized by high emissivity (~100%), introduce undesired Poisson noise; however, through proper design of a cold stop in the IR science instrument, such contamination should be masked effectively.

It is expected that thermal background will limit the maximum exposure time (due to saturation, especially at longer wavelengths), so that the required time on source will be achieved through coaddition of short exposures.

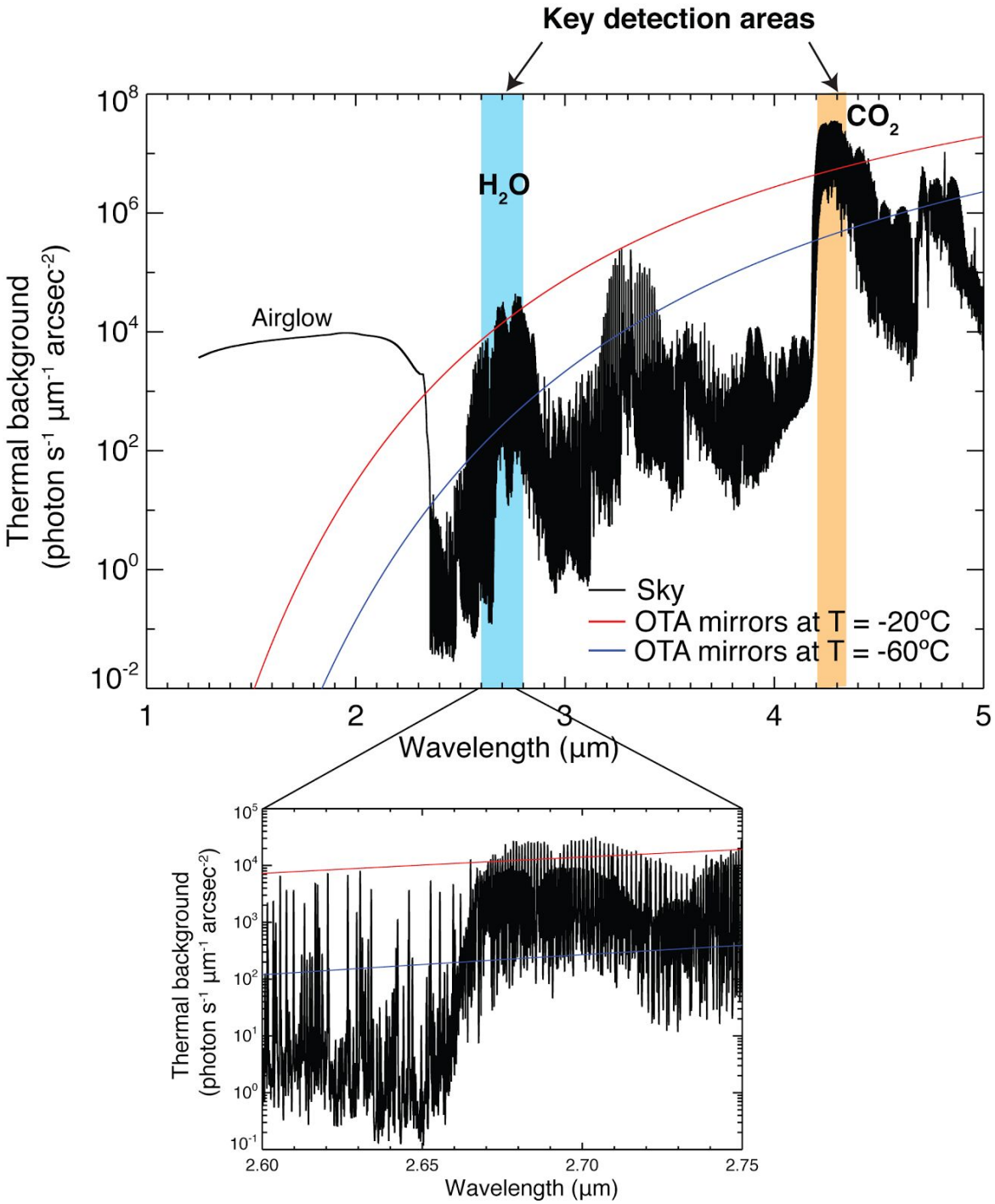

Figure 9. Estimate of thermal contribution from Earth's atmosphere, airglow, and GHAPS primary and secondary mirrors at Cassegrain focus. Top: Model comparison of thermal background emitted by the atmosphere (using the Line-By-Line Radiative Transfer Model; Clough et al. 2005) and airglow (Leinert et al. 1998) vs. thermal flux emitted by the combined primary and secondary mirrors at temperatures -60 ºC and -20 ºC (assuming mirror emissivity of 5%, telescope throughput of 90%, and a spectral resolving power of 20,000). Bottom: Zoom of the 2.60-2.75 µm range where water emission lines are detected in fundamental ro-vibrational bands. The near-infrared zenith airglow

measurements below 2.4 μm (at low resolution) performed from a balloon at 30 km altitude during flights in 1972 and 1974 (Leinert et al. 1998 and references therein) are considered. Such low resolution airglow measurements characterize what would be a forest of lines at high resolution. Given such uncertainties, we opt to neglect airglow contribution beyond 2.4 μm.

4.3. General Instrument Classes

There is a wide range of science cases for which balloon-borne measurements can make particularly significant contributions. As mentioned earlier, many of these cases were discussed in Dankanich et al. (2016), so this document does not attempt to comprehensively review those science investigations. Rather, we discuss several *example* science cases and present notional instruments that can achieve such objectives. Table 3 lists the main characteristics of GHAPS science instrument types. We anticipate that these types of instruments will provide their own calibration techniques to ensure that the photometric/radiometric accuracy is met to achieve the intended science objectives.

Table 3. Notional GHAPS instrument classes.

Instrument Class	Wavelength (μm)	Detector type	Detector temperature	Guided
UV-Vis Imagers and Spectrometers	0.2 - 0.9	Si-based photodiodes, CMOS, and CCDs, GaP, Ge, InGaAs, PbS Photomultiplier, MCT (PV)	cooled	yes
NIR Imagers and Spectrometers	0.9 - 5	InSb, InAs, PbS, PbSe, MCT (PV)	cooled	yes/no[1]
MIR Imagers and Spectrometers	5 - 17	MCT (PC), VOx and Si microbolometers, thermopiles, pyroelectrics	Cooled and uncooled	no
Thermal Imagers and Radiometers	> 17	Thermopiles, Pyros, Ge and Si bolometers	Cooled and uncooled	no

[1] Some NIR applications may require pointing that can be provided by the GHAPS OTA itself, which is expected to keep the entire telescope on target at the ~1” level. Other NIR applications may require an additional level of stability to be provided by the instrument.

5. Potential Science Drivers

5.1. Optical / UV Spectral Region

5.1.1 Kuiper Belt Object, Near-Earth Object, and Asteroid Binaries

Binary (and higher-order) companions of minor planets provide a unique pathway to measuring the bulk properties of their primaries. In the absence of extremely high-precision absolute astrometry, system mass can still be determined by a binary orbit, and in higher-multiplicity systems the component masses can be extracted. Given that GHAPS imagery will benefit from the complete Gaia astrometric catalog, a GHAPS imager may be able to provide the extremely high-precision absolute astrometry required to measure binary component masses. This is contingent on the GHAPS UV-Vis imager having the properties of a wide-field high-precision astrometric instrument (a stable, critically-sampled focal plane, high dynamic range, high-speed global shutter, characterizable distortion terms, and characterizable intra-pixel sensitivities). Additionally, to fully leverage the astrometric potential of a GHAPS UV-Vis imager for NEO and main belt asteroid observations, shutter open and close times must be recorded with absolute accuracy and precision better than a millisecond. GHAPS capabilities for high-precision absolute astrometry can exceed those of larger ground-based extreme-AO systems given its potential wide diffraction-limited field of view, over which many astrometric reference stars can be imaged simultaneously. While speckle interferometry on large-aperture facilities can also deliver high-contrast images, it is not suitable for high-precision absolute astrometry and its low sensitivity limits its applicability to faint minor planet populations.

GHAPS capabilities for high-precision absolute astrometry can exceed those of larger ground-based extreme-AO systems given its potential wide diffraction-limited field of view, over which many astrometric reference stars can be imaged simultaneously.

Higher-order bulk properties can also be probed with multiple systems. The orbits of the companions of asteroid (87) Sylvia, in combination with a 3D shape model of the primary, suggest that its interior is non-homogenous, perhaps a signature of differentiation (Berthier et al. 2014). A GHAPS UV-Vis imager could provide the high-contrast, high-acuity imagery capable of separating the components of a Sylvia-like system (0.2”–1” separations, 6.24–7.2 magnitude contrast) if the wavefront error budget of the imager does not drive the total system’s wavefront error budget significantly beyond the OTA specification of ~λ/20 (Fig. 10). There are a number of multiple systems accessible to GHAPS that have not yet been characterized to the degree of (87) Sylvia, including (3749) Balam and (2577) Litva, both triples.

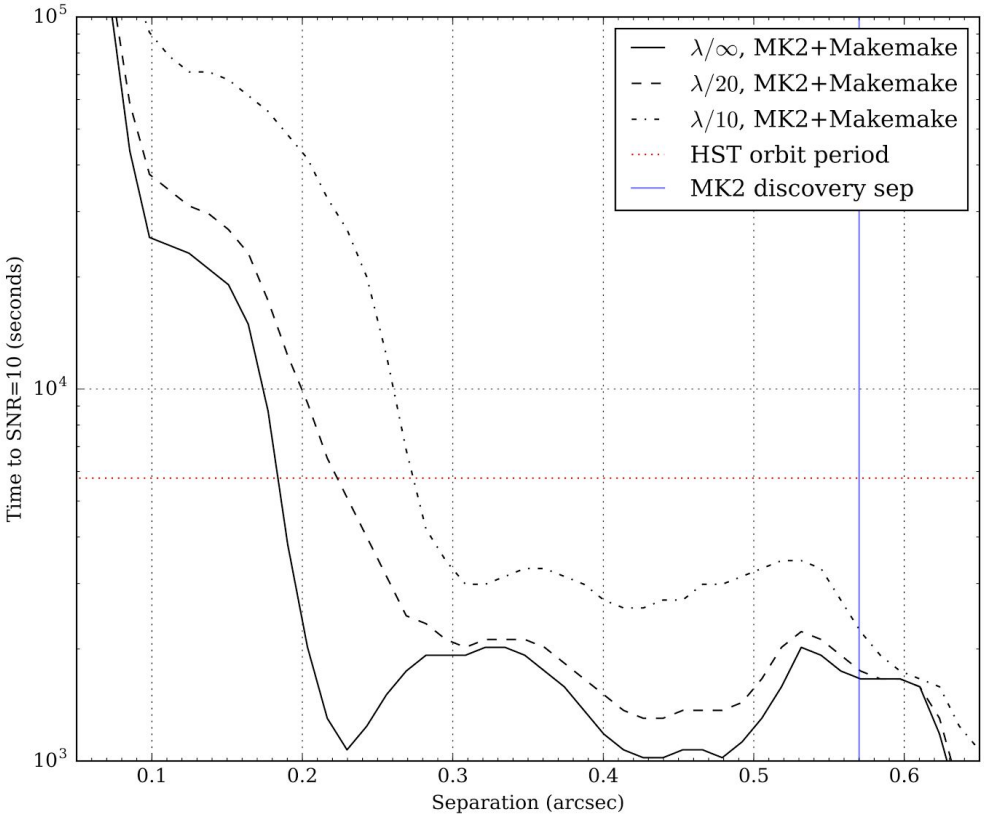

Figure 10. Example of effect of degrading GHAPS PSF quality on high-contrast imaging. Simulation of time to achieve signal-to-noise = 10 for a S/2015 (136472) 1-like satellite ("MK2") around the dwarf planet Makemake (V~17) as a function of separation; system has a 1300:1 contrast ratio. Results for a model monochromatic PSF at 500 nm with a GHAPS-like optical system and central obscuration (but no secondary support vanes) are illustrated for an ideal PSF, target spec PSF, and half-spec PSF. For tight inner working angles (~0.2"), a half-spec PSF increases required integration time by nearly a factor of five or the target specification. SNR estimates based upon a V-band filter bandpass and sky surface brightness of 21 magnitudes per square arcsecond.

A GHAPS UV-Vis imager would also be capable of discovery and characterization of new binary companions for minor planets across the solar system. Kuiper Belt dwarf planets have an extremely high binary fraction (e.g., Parker et al. 2016), and their companions tend to be relatively small compared to their primaries and in tight orbits. Smaller classical Cold Classical Kuiper Belt Objects (CCKBOs) have perhaps the highest binary fraction of any minor planet population, with physical properties unique in the solar system. These binary systems tend to be nearly equal-mass, and the population extends to very wide separations. The distribution of binary properties and the population-resolved binary fraction are powerful indicators of formation and evolution processes, which are directly coupled to planetesimal formation and evolution processes (Schlichting & Sari 2008, Nesvorny et al. 2010, Parker et al. 2011, Parker & Kavelaars 2012). A survey for tight

binary companions of *every* CCKBO discovered in the well-characterized Canada France Ecliptic Plane Survey (CFEPS) and Outer Solar System Origins Survey (OSSOS, currently >200 CCKBOs, expectation for >300 when OSSOS complete) could be performed in a small fraction of two GHAPS flights (requiring two flights only to access the full range of ecliptic longitudes). GHAPS could also easily provide follow-up sufficient to measure the orbital properties of all (~50) discovered binary systems within a reasonable allocation of time. Wide KBO binary systems can have mutual orbit periods ranging from days to over 10 years (Parker et al. 2011), requiring low-frequency repeat observations over several-year timescales to fully measure their orbital properties; measurement of orbit poles requires several years even for short mutual orbital periods.

Since the observed CCKBO binary fraction is seen to rise rapidly with decreasing separation (Kern & Elliot 2006), the optical performance of the GHAPS OTA must not be compromised by the UV-Vis imager. Low wavefront error, high-performance guiding (~30 milliarcsecond RMS), and a critically-sampled focal plane are required to preserve and record the diffraction-limited image quality of ~0.1"; degradation of this image quality or sampling will rapidly reduce the sensitivity of GHAPS to close, faint binary companions. Characterizing the orbital properties of a binary system requires accurate WCS solutions for resolved images of the system; a several-arcminute FOV is typically large enough to ensure that a sufficiently large number of astrometric reference catalog stars are available to determine a WCS solution. Given a 180" FOV, the Gaia catalog will contain a sky-averaged ~30 stars per FOV. At a galactic latitude of 60º, this reduces to ~5 stars per 180" FOV.

Figure 10 illustrates the effect of increasing the wavefront error of a UV-Vis system beyond the GHAPS OTA spec of ~λ/20 on high-contrast imaging of small satellites; in this case, Makemake and its satellite S/2015 (136472) 1. Currently, only HST is an efficient platform to recover and characterize the orbit of S/2015 (136472) 1; GHAPS could provide an alternative platform for such observations. However, the time required for separating S/2015 (136472) 1 from Makemake for tight inner working angles depends strongly upon the total wavefront error budget of the combined GHAPS OTA + UV-Vis imager. Increasing the total wavefront error budget to λ/10 increases the required integration time to achieve SNR ~ 10 by more than a factor of four. Thus efficient high-contrast observations (which permit searching for faint companions near bright primaries in minor planet populations across the solar system) are enabled by maintaining the system wavefront error budget of the OTA + UV-Vis close to ~λ/20.

Near Earth Objects (NEOs) frequently host small companions, often discovered via RADAR observations. GHAPS UV-Vis high angular resolution imaging (and imaging spectroscopy) during NEO flybys would permit both discovery of these companions and characterization of their spectral properties, a capability complementary to radar characterization. Such systems are of interest for In Situ Resource Utilization (ISRU), human exploration, and planetary defense. This capability is contingent upon UV-Vis imaging (or imaging spectrometry) instruments having sufficient measurement capabilities, and the additional requirement that the instrument's fine guiding system can deliver high angular rate guiding. While typical fast NEO non-sidereal rates of motion are of order 2 degrees per day, very close NEO flybys frequently exhibit angular rates of motion of several tens of degrees per hour. The performance of the GHAPS platform's

tracking at these high non-sidereal rates is unknown at present, and any UV-Vis imager operating at these rates may have to compensate for larger guiding jitter than the ~arcsecond RMS GHAPS baseline specifications.

Table 4. Measurement requirements for KBO and asteroid binary science case.

Parameter	**Requirements**
Field of View	~3 arcmin
Filters/Wavelength Coverage	Medium- to Broad-band optical (Johnson- or SDSS-like.)
Spectral Resolution	N/A
1D, 2D, or Multi-Object Spectroscopy?	N/A
Spatial Resolution	Diffraction limited at 500 nm (FWHM~0.12”); high-strehl PSF (~λ/20 WFE budget); critically-sampled (or better) PSF.
Guiding / Pointing Performance	Jitter < ~30 mas RMS; high non-sidereal guiding rate (for NEOs, >2 degrees/day minimum)
Sensitivity/Associated SNR	N/A
Cadence/Duty Cycle/Total Experiment Duration	KBOs: Cadence: 1/day - 1/quarter. Duty cycle: N/A. Duration: years NEOs: Cadence: Minutes. Duty cycle: N/A Duration: hours
Subsystem Temperatures	N/A

5.1.2 Venus cloud top characterization

Two outstanding science questions related to the atmosphere of Venus in which balloon-borne observations can make significant contributions are (a) the identity of the unknown “mystery” UV absorber present in Venus’ uppermost cloud deck, and (b) the cause of its atmospheric superrotation. Esposito et al. (1997) suggested that an unidentified absorption feature in Venus’ UV spectrum could be caused by sulfur allotropes, S_2O, $FeCl_3$, or some combination thereof. The identity of this absorber is important because the absorption of sunlight in this spectral region strongly influences Venus’ energy balance and atmospheric dynamics. Recent narrowband UV (365 nm) imaging observations with the Venus Monitoring Camera on the *Venus Express* orbiter suggest that the unknown absorbers are small particles of concentrated sulfuric acid mixed with one of the aforementioned candidate materials (Markiewicz et al. 2014;

Petrova et al. 2015). Imaging Venus in the UV through a wide range of phase angles, which is impossible using ground-based telescopes, will further elucidate the scattering properties of these aerosols and will lead to an improved understanding of the identity of the mysterious UV absorber.

A balloon-borne platform is also ideally suited for investigating Venus' atmospheric circulation. The cloud tops of Venus circulate around the planet in a mere 3-5 days while the surface slowly rotates underneath over a 243 day period. Previous cloud-tracking efforts using UV observations by the *Galileo*, *Pioneer Venus* orbiter, and *Venus Express* spacecraft revealed large-scale wind fields and wave phenomena (Limaye et al. 1988, Peralta et al. 2007, Markiewicz et al. 2007), and variations in the zonal and meridional cloud-top winds on timescales of years, days, and hours (Khatuntsev et al. 2013). Balloon-borne measurements of cloud motions on Venus can fill an important niche in terms of both temporal and spectral coverage that are inaccessible from other platforms. This will lead to an improved understanding of Venus' global circulation patterns and the processes that control that planet's climate.

The angular size of Venus ranges from ~ 10" at superior conjunction, when it is in a nearly "full" phase, to roughly 60" at inferior conjunction, when it is a thin crescent with almost none of the illuminated hemisphere facing towards Earth. At maximum elongation, when the angular separation between Venus and the Sun is maximized, the angular size of Venus is ~ 30" and cloud features will move detectably over hour timescales. Near-UV images acquired over timescales of minutes to hours can be used to track the motions of Venus' cloud tops, including both zonal and meridional flows, in an effort to accurately map the high altitude wind field. This can be linked to deeper atmospheric flows, which can be derived from measurements made using near-IR images at 1.7 and 2.3 μm obtained from ground-based facilities or the JAXA Venus orbiter *Akatsuki*. Short wavelength imaging offers the unique capability to measure wind speeds at altitudes not obtainable from ground-based observations. Integration times of several seconds would be sufficient to achieve a signal-to-noise of 100 or greater. Furthermore, GHAPS will deliver the ability to achieve 0.5" image quality at short wavelengths for an object that is frequently at a low elevation angle. Because the angular separation between Venus and the Sun is never more than ~ 45º, it is a prime candidate for daytime observations, which will be enabled by GHAPS.

Because the angular separation between Venus and the Sun is never more than ~ 45º, it is a prime candidate for daytime observations.

Table 5. Measurement requirements for Venus winds science case.

Parameter	Requirements
Field of View	1 arcmin or greater
Filters/Wavelength Coverage	near-UV (365 nm)
Spectral Resolution	Narrowband (dλ ~ 35 nm)

1D, 2D, or Multi-Object Spectroscopy?	none
Spatial Resolution	~ 200 km/pix
Guiding / Pointing Performance	0.5 arcsec
Sensitivity/Associated SNR	SNR ~ 100
Cadence/Duty Cycle/Total Experiment Duration	t_{exp} ~ 5 sec; multiwavelength images taken every 30 minutes for total duration of ~ 4 days
Subsystem Temperatures	N/A

5.1.3 Cloud tracking on ice and gas giants

Imaging the atmospheres of the giant planets at UV and visible wavelengths can enhance our understanding of their coupled chemical and dynamical processes. It is common to use infrared spectral image cubes to probe planetary atmospheres at different depths, using the variations in opacity due to CH_4 or other constituents. Opacities in visible wavelengths are generally weak overtones of IR absorptions, and visible wavelength spectral image cubes can therefore probe higher altitudes than those resolved by IR image cubes alone. In addition, the giant planet atmospheres have hazes that scatter light much more effectively at visible than IR wavelengths, so a balloon-borne telescope could provide high-spatial resolution imaging that is diagnostic of haze abundances.

The gas giant planets Jupiter and Saturn exhibit atmospheric dynamics as manifested through cloud motions on a wide range of spatial and temporal scales. Near-UV, visible and VNIR images of the gas giants can provide windows to a variety of physical processes. In the near UV Rayleigh scattering begins to dominate and observations are most sensitive to the stratospheric hazes located near the poles. Blue wavelengths probe signatures of the reddish colored regions in Jupiter's atmosphere (e.g. the Great Red Spot), which appear red because they are highly absorbing in the blue. The red to VNIR spectral region covers the methane absorption bands at 619, 727, and 890 nm (in order of increasing strength). These increasingly strong methane absorption bands enable vertical discrimination in the atmospheres of Jupiter and Saturn, hence cloud tracking measurements made at these different wavelengths can provide clues into the variation of wind speed with height.

Furthermore, the ice giants Uranus and Neptune have displayed increased cloud activity over the past decade (Fig. 11), and the degree to which this is related to seasonal variations in insolation can be explored using optical imaging taken at a time cadence that allows complete longitudinal coverage. The rotational periods of Jupiter, Saturn, Uranus, and Neptune are roughly 9.9, 10.5, 17.2 and 16.1 hours, respectively, hence it is difficult or impossible to observe complete rotations of the giant planets from ground-based or HST observations. Neptune, in particular, is extremely variable on short time scales

(days), and better temporal coverage over these timescales is required to understand the energetics and motions of storm development and dissipation. Maximum contrast for Neptune and Uranus is in the red, where the planets are darker due to methane absorption.

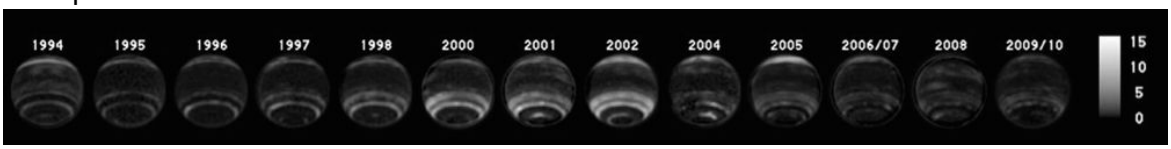

Figure 11. Images showing the annual averages of cloud filling factors on Neptune, computing from HST images taken between 1994–2010 through filters spanning 344–843 nm (Karkoschka 2011).

The rotational periods of Jupiter, Saturn, Uranus, and Neptune are approximately 9.9, 10.5, 17.2 and 16.1 hours, respectively, hence it is difficult or impossible to observe complete rotations of the giant planets from ground-based or HST observations.

Table 6. Measurement requirements for giant planet cloud tracking science case.

Parameter	**Requirements**
Field of View	1 arcmin
Filters/Wavelength Coverage	UV-Vis narrowband (specific filters to match HST/WFPC2)
Spectral Resolution	Narrowband
1D, 2D, or Multi-Object Spectroscopy?	IFU or hyperspectral imaging desirable for Jupiter and Saturn to get spatially resolved spectra at various locations across the disk
Spatial Resolution	Diffraction limited
Guiding / Pointing Performance	Jitter ~30 mas (RMS)
Sensitivity/Associated SNR	SNR ~ 5–100
Cadence/Duty Cycle/Total Experiment Duration	t_{exp} ~ 5–30 sec depending on target; multiwavelength images taken every 10–20 minutes for total duration of ~ 4 days
Subsystem Temperatures	N/A

5.1.4 Asteroid space weathering and resurfacing

The surfaces of airless bodies in our solar system are constantly being modified by exogenous processes that affect their compositions, and which can be characterized through multi-spectral UV-Vis imaging. This 'space weathering' changes the UV-Vis spectrum of surfaces by decreasing the depth of crystal field transition absorption bands and the UV-Vis slope resulting from oxygen-metal charge transfer absorptions, especially in minerals bearing transition elements such as iron (Fig. 12). Because the Oxygen-Metal Charge Transfer (OMCT) band is particularly strong in the UV-Vis, multiple spectral measurements from ~ 200 nm to 500 nm are capable of characterizing surfaces that are more or less weathered, providing information on surface age, exposure time, and composition. A balloon-borne platform enables imaging at wavelengths not available from the ground in the UV and NUV. Additionally, the lower scattered light at high airmass enables observations of objects closer to the Sun than possible with ground based telescopes, thus enabling some observations immediately after sunset. For instance, multi-spectral measurements of main belt asteroids at 200 nm, 300 nm, 320 nm, and longer, with spectral widths of a few 10s of nanometers would be able to characterize the OMCT band in oxides and silicates at signal-to-noise of a few 10s to 100 for integrations times of seconds to minutes; for U=18, a 20 second exposure should achieve SNR>50.

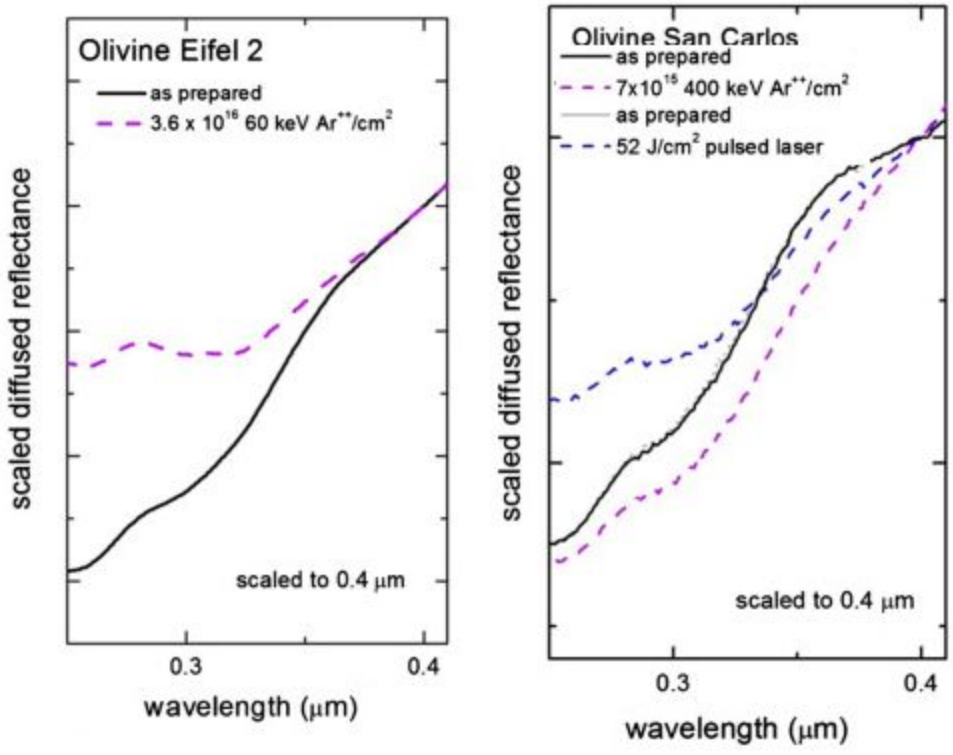

.

Figure 12. UV bluing of silicate minerals 'weathered' in the laboratory with ion bombardment and laser irradiation. Based on Fig. 2 in Kanuchova et al. (2015).

High guiding rate performance could enable unique observations of fast-moving NEOs. For example, during the 2029 flyby of (99942) Apophis, GHAPS could deliver resolved UV-Vis images of the asteroid (~20 resolution elements across the ~2" width of the disk; V-band surface brightness <5 magnitudes / arcsecond at flyby, or V ~11.5 per 0.05" nominal UV-Vis pixel; GHAPS can deliver SNR > 30 per pixel in a 10 ms exposure) provided the UV-Vis guider can perform at non-sidereal tracking rates of 40º/hr. Encounters with planets similar to the 2029 flyby of (99942) Apophis are expected to modify the properties of asteroids, potentially reshaping them, revealing less-weathered material, and/or changing their spin state (e.g., Richardson et al. 1998, Keane and Matsuyama 2014). Measuring the properties of small asteroids before, during, and after close approach may permit the detection of material changes, through changes in spectral properties or lightcurve properties (Keane and Matsuyama 2014).

Table 7. Measurement requirements for asteroid space weathering science case.

Parameter	**Requirements**
Field of View	>20" to enable nodding
Filters/Wavelength Coverage	200–800 nm Space weathering: Narrowband (10–50 nm) Structural changes: Broadband, F350LP-like
Spectral Resolution	~ 10 (if narrowband)
1D, 2D, or Multi-Object Spectroscopy?	1D
Spatial Resolution	Space weathering: FWHM<1" Structural changes: Diffraction limited at 500 nm (FWHM ~ 0.12"); high-strehl PSF (~λ/20 WFE budget)
Guiding / Pointing Performance	Structural changes: Jitter < ~30 mas (RMS); high non-sidereal guiding rate (for Apophis-like flyby, >40 º/hr)
Sensitivity/Associated SNR	Structural changes: SNR~10 for surface brightness ~5 magnitudes / arcsecond
Cadence/Duty Cycle/Total Experiment Duration	Structural changes: 100

	ms cadence, ~50% duty cycle, Total experiment duration of ~hours
Subsystem Temperatures	N/A

5.1.5 SO_2 and Volcanism on Io and Venus

Atmospheric SO_2 is thought to trace epochs of volcanism on Venus, since it is known to be a product of volcanism on Io. Monitoring UV SO_2 lines is therefore a powerful tool for tracking volcanism on these two worlds. Tsang et al. (2013) demonstrated recovery of time-variable SO_2 abundances in Io's atmosphere using a combination of 210-235 nm HST COS UV spectroscopy and IRTF MIR spectroscopy. Continuum levels detected by HST COS were ~10^{-7} W/m^2/A; scaling from COS sensitivities, an R~1000 GHAPS UV imaging spectrometer should be able to deliver detections of comparable signal-to-noise in integration times of order 10,000 seconds, depending on float altitude. GHAPS' imaging acuity would permit of order 100 spatial resolution elements on Io's disk, allowing spatially-resolved mapping of atmospheric SO_2. Extending wavelength coverage to 270-320 nm provides additional coverage of SO_2 features used to probe the composition of Venus' atmosphere; imaging spectroscopy across Venus' disk would permit continued monitoring of putative large-scale volcanic activity (Marcq et al. 2011, 2013), and potentially help in localizing SO_2 sources. The UV spectral windows of ~ 200 - 225 nm and ~ 280 nm to the visible that are available at float altitude span a sufficiently large portion of these features to enable this measurement.

Table 8. Measurement requirements for Io and Venus SO_2 and volcanism science case.

Parameter	**Requirements**
Field of View	several arcseconds (Io) to 1 arcmin (Venus)
Filters/Wavelength Coverage	210-235 nm; 270-320 nm
Spectral Resolution	R ~ 1000
1D, 2D, or Multi-Object Spectroscopy?	Imaging spectroscopy over Io disk (~1.5" diameter) and Venus disk (tens of arcseconds)
Spatial Resolution	Diffraction limited
Guiding / Pointing Performance	Jitter < ~30 mas (RMS)
Sensitivity/Associated SNR	SNR ~10 per spectral

	element at 10^{-17} W/m^2/A
Cadence/Duty Cycle/Total Experiment Duration	Revisits on 2-3 hour timescale for several days to sample range of sub-observer latitudes.
Subsystem Temperatures	N/A

5.2. Near IR through Mid-Wave IR

5.2.1 Jupiter's Aurorae

The NIR-MIR wavelength range between 3 and 8 μm, accessible to an instrument on GHAPS, permits investigation of aurorae on the outer planets. Aurorae occur at the intersection of atmosphere and magnetosphere, where energetic particles are accelerated by potential differences along magnetic field lines and beam into the neutral atmosphere, creating a remotely detectable diagnostic for magnetospheric processes, both internal such as the fueling of Jupiter's magnetospheric plasma by its satellite Io, and external such as variable solar wind plasma pressure.

Jupiter is the most powerful auroral phenomenon in the solar system, and studies of auroral phenomena at different wavelengths, spanning from X-ray through radio, allow the investigation of energy deposition vs altitude. For instance, the near-infrared emission of the molecular radical H_3^+ at 3.4 μm is found in Jupiter's upper atmosphere, above the homopause, and the mid-infrared emission of hydrocarbon species such as methane, ethane, ethylene, and acetylene provides information below the homopause. Indeed, only minor segments of the H_3^+ v_2 emission band are accessible from the ground, due to telluric water and methane opacity, yet it is uniquely accessed by GHAPS, thus yielding a direct measure of energy deposition in the upper atmosphere. Furthermore, the methane v_4 band at 7.8 μm and the acetylene Q-branch emission at 13 μm can probe processes throughout the auroral column.

GHAPS can yield investigation of aurorae on the outer planets through observations of the H_3^+ (v_2 band) at 3.4 μm, methane (v_4 band) at 7.8 μm and the acetylene (Q-branch) at 13 μm, which is precluded from the ground due to telluric water and methane opacity.

Although spatial resolution is important, the auroral emission is spatially distributed and thus resolving it is not essential to its detection; the 1 m telescope aperture ensures the emission is not under resolved. Above this baseline aperture, the limb of the planet is the primary discriminator for the segment of auroral emission that is detectable. The critical feature provided by GHAPS is wavelength coverage in the 3.4 μm band and from 4 to 8 μm with spectral resolving power R ~ 500. Isolated minor portions of the H_3^+ v_2 emission

band are observed from ground, yet absolute calibration is difficult. GHAPS can capture the entire band, spectroscopically (R ~ 300 – 1000) or through spectro-imaging (R ~ 30 to capture entire band) using hyperspectral, dispersive grating, Fabry-Perot or narrow band filter instrumentation. Jupiter rotation creates a modulation that varies continuously, so continuous measurements or rapid switching between spectral channels (filters) is preferable — Jupiter aurorae can vary on timescales of minutes or hours. Simultaneous or near-simultaneous measurements can precisely determine the variation timescale.

Table 9. Measurement requirements for Jovian aurorae science case.

Parameter	**Requirements**
Field of View	1 x 1 arcmin (Jupiter is ~43 arcsec diameter)
Filters/Wavelength Coverage	3.4 μm ± 100 nm and 4 to 8 μm filters
Spectral Resolution	~R = 500 (1–5 μm spectroscopy) ~R = 30 (imaging)
1D, 2D, or Multi-Object Spectroscopy?	2-D or hyperspectral Imaging spectroscopy
Spatial Resolution	Diffraction limited; ~12 resolution pixels at 3.4 μm (~1 arcsec)
Guiding / Pointing Performance	~0.5 arcsec
Sensitivity/Associated SNR	SNR > 15
Cadence/Duty Cycle/Total Experiment Duration	Minutes to hours
Subsystem Temperatures	OTA mirrors ~ 230 K

5.2.2 Variability of Lunar Water

In 2009 Deep Impact detected hydrated mineral exposures on the Moon over all spatial scales (Fig. 13). Such measurement of lunar water at ~2.8 μm required an integration time (on target) of ~0.1 sec at a resolving power R ~ 300. One of the most surprising and important aspects of lunar hydration was the observation of apparent diurnal variability in the degree of hydration by Sunshine et al. (2009), countered by Clark (2009) as possibly only a result of optical scattering processes from a uniform hydration layer but variable phase angle. Later evidence from distinctly different methodologies (Hendrix et al. 2012;

Livengood et al. 2015) supported the contention of diurnal variability, but with controversial implications for the quantity of water.

Thanks to the minimal terrestrial water absorption, this is an important research area that can be explored by GHAPS. Investigation of phase angle and local time effects on hydration content can probe possible processes controlling the delivery and transport of water at the Moon's surface.

Resolving power R ~ 300, or spectral resolution ~ 0.01 μm at 3 μm, would be valuable to distinguish the phase of observed water, as the chemical state shifts the asymmetric fundamental band in frequency, from ~ 2.80 to 2.85 μm in disordered hydroxylated minerals, to 2.95 μm in water (including adsorbed molecular water), and to 3.05 μm for bulk water ice. While water ice does not exist on the illuminated portions of the Moon, adsorbed molecular water may be present at high latitudes (Hibbitts et al., 2011, Poston et al., 2013), possibly detected in some Chandrayaan-1 M3 observations (McCord & Combe, 2010). Spectroscopy at R ~ 300 can distinguish H_2O from OH hydration, as this fundamental information is not yet known and conceivably could be spatially or temporally variable, depending on the physical environment in which water-group species are delivered or persist. Filter imaging with carefully selected wavelengths that have similar full width half maximum in-band transmission, but very good out of band rejection (~ OD 4 average) can also make this measurement. The diffraction limit of a 1 m telescope at 3 μm is 0.75 arcsec (Rayleigh criterion), which projects to 1.4 km at the Moon. This is quite sufficient to measure local-time dependence, since one hour of local time projects to 455 km at the Moon's surface. Individual patches of terrain can be tracked through the lunar cycle from dawn to dusk, to investigate variability.

Spectroscopy at R ~ 300 can yield studies of lunar hydration processes, allowing the distinction of H_2O from OH hydration. Individual patches of terrain can be tracked through the lunar cycle from dawn to dusk, to investigate variability.

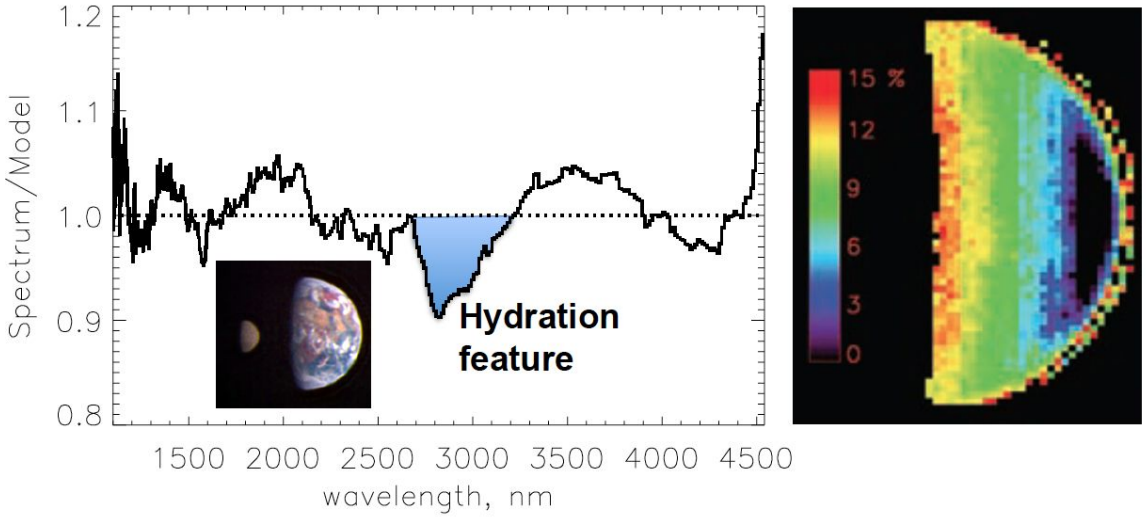

Figure 13. Spectroscopic detection of lunar mineral hydration. (Left) 2.8 μm feature in disc-integrated 1–5 μm spectrum divided by a model for reflectance plus thermal emission, from the pictured observation in a May 2008 transit of Earth by the Moon (Livengood et al. 2011). (Right) Map of lunar hydration feature band depth in June 2009, looking down on the north pole, showing strongest hydration at terminator; reprinted from Sunshine et al. (2009).

Table 10. Measurement requirements for the variability of Lunar water science case.

Parameter	Requirements
Field of View	~3 x 3 arcmin (for image mosaicing)
Filters/Wavelength Coverage	2.5 to 3.8 μm (long wavelength required for thermal correction)
Spectral Resolution	~R = 300 (2.5 - 5 μm spectroscopy) ~R =10 (narrow band filters)
1D, 2D, or Multi-Object Spectroscopy?	Imaging Spectroscopy or Multispectral Imaging
Spatial Resolution	0.75 arcsec (1.4 km)
Guiding / Pointing Performance	~0.5 arcsec
Sensitivity/Associated SNR	SNR > 100
Cadence/Duty Cycle/Total Experiment Duration	0.05 s to 10 s exposures on a daily basis for a lunation or preferably longer
Subsystem Temperatures	Cold MCT detector focal plane

5.2.3 Organics and Volatiles on Asteroids

The 2.5–5 μm region is sensitive to the fundamental vibrational absorption features associated with volatile and organic compounds that can be present in the surfaces of asteroids, such as water (2.95 – 3.05 μm), hydroxyl (2.7 – 2.85 μm), hydrocarbons (3.2 - 3.5 μm), carbon dioxide (4.25 μm), carbon monoxide (4.6 – 4.7 μm), cyanogens (~ 4.6

μm), and absorption features in alteration minerals such as carbonates (3.8 – 4 μm). A significant component of the Earth's volatiles and prebiotic organic molecules, and those of the terrestrial planets, may have originated from asteroidal material. Yet there is not a clear understanding of the organic and volatile composition of this asteroidal reservoir — including NEAs, Main Belt and Trojan asteroids. Some asteroids are remnant building blocks from the early solar system, others are shards from recent collisions. Their compositions are known to vary widely; some are highly desiccated silicates, some are hydrated, and some quite volatile rich. But there is little understanding of the specific volatile and organic mineralogy. Understanding this composition would help us understand the origin and evolution of the inner solar system, especially of prebiotic materials. Examples of the value of this measurement are the spectra of Vesta (e.g. McCord et al., 2012) and Ceres (DeSanctis et al., 2015). Both bodies contain C-type materials on their surfaces (a surprise for Vesta), with Ceres containing some materials previously detected (e.g Rivkin et al., 2006) and other materials not previously known to exist on its surface. These spectral features of these condensed phase materials can be well characterized with R of several hundred in the 2.5 to 5 μm range. At 14th magnitude, approximately 230 asteroids will regularly be available.

Table 11. Measurement requirements for asteroid organics and volatiles science case.

Parameter	**Requirements**
Field of View	> 10" to enable nodding
Filters/Wavelength Coverage	2.5 to 5 μm
Spectral Resolution	< 20 nm for organics, < 50 nm for water
1D, 2D, or Multi-Object Spectroscopy?	N/A
Spatial Resolution	Diffraction limited
Guiding / Pointing Performance	Jitter: < 0.1 arcsec during a single integration Drift: < 0.1 arcsec during a single integration
Sensitivity/Associated SNR	SNR ~ 100 at V = 14
Cadence/Duty Cycle/Total Experiment Duration	Measurement Dependent
Subsystem Temperatures	OTA: ~< 230K Detector: Instr. specific

5.2.4. Volatiles in Comets

5.2.4.1 Carbon dioxide (CO_2)

Observed activity in comets at large heliocentric distances (e.g., > 3 AU) has traditionally been attributed to species more volatile than H_2O, with CO and/or CO_2 being the most likely candidates. The abundance ratio CO/H_2O varies by more than 2 orders of magnitude (from < 1 to ~ 20%) among more than 20 measured Oort cloud comets, however comets with high CO/H_2O (> 10%) are relatively few in number (Paganini et al. 2014). The Japanese *AKARI* mission surveyed 18 comets spectroscopically between 2008 – 2010 (Ootsubo et al. 2012), encompassing fundamental emission bands of H_2O, CO_2, and CO in the 2.5 – 5.0 μm wavelength range. H_2O and CO_2 were measured in 17 of these, CO_2 was more abundant than CO in approximately half of those surveyed, and CO_2/H_2O varied between ~ 5 – 30% among comets within 2.5 AU of the Sun. The *AKARI* results, plus measurements of three comets by the Deep Impact/DIXI mission between 2005 and 2012 (Feaga et al. 2014, A'Hearn et al. 2011, Feaga et al. 2007) spurred a major paradigm shift regarding the prominent role of CO_2 among cometary ices. This provides compelling incentive for continued measurements of CO_2 in future comets.

Within a few years, JWST will provide a means of measuring cometary CO_2 from space. However, the highest spectral resolving power (R ~ 3000) of its IR spectrometer (NIRSpec) is insufficient for conducting line-by-line studies. Furthermore, solar avoidance restrictions and overall demand for astronomical observations will limit its availability to conduct comet science. As a dedicated facility for planetary science, GHAPS can provide a viable alternative platform for carrying out such studies.

As a dedicated facility for planetary science, GHAPS can provide unique studies of CO_2 and potentially the first direct detection and chemical survey of CO_2 from the Earth environment. This is not feasible from ground-based observatories.

Lines of the strong fundamental band (v_3) of CO_2 are completely blocked from ground-based telescopes, owing to atmospheric opacity (Fig. 14, bottom panel). Even from 35 km altitude, the cores of telluric v_3 absorptions are opaque. However, for comets having relatively large CO_2 production rates, measurement of CO_2 is possible even at small radial velocities (Delta-dot) between the comet and Earth (Fig. 14, top panel).

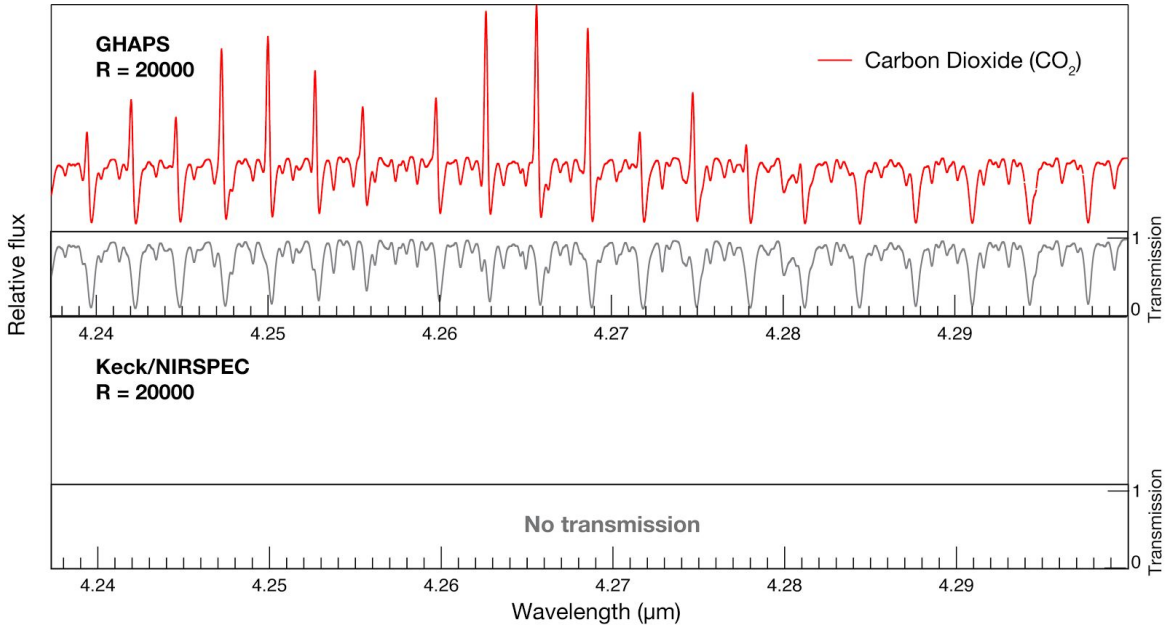

Figure 14. Model of carbon dioxide emission from a comet at 1 AU heliocentric and geocentric distance, assuming a CO_2 production rate of 5 x 10^{27} molecules s^{-1} and a geocentric velocity (Delta-dot) of -5 km s^{-1}. Top panel: The transmittance function at 35 km altitude enables sensing of CO_2 molecules in its strong (v_3) band. Bottom panel: Ground-based sensing of CO_2 is precluded by strong carbon dioxide absorption in Earth's atmosphere throughout this spectral region.

This capability is demonstrated in Figure 15 for GHAPS altitude and for several values of Delta-dot, and shows the dramatic improvement in atmospheric transmittance as cometary CO_2 emission lines are Doppler-shifted away from the cores of corresponding telluric v_3 absorptions. At Delta-dot = -10 km s^{-1} (panel B) we estimate a SNR of 10 in the brightest lines in 1 hour of on-source integration time for a comet with CO_2 production rate ~ 3 x 10^{26} molecules s^{-1}. This estimate, and also that for H_2O (see § 5.2.4.3) assume a 5-pixel (~ 1.33 arc-second) wide slit, and are based on signal summed over 5 spatial pixels centered on the comet. Our estimates include corrections for (1) background subtraction, and (2) loss of flux, not captured in the slit based on the nominal (diffraction limited) PSF. Together these two corrections are assumed to introduce an additional factor of approximately two to the limiting 10-σ line flux. Additionally, and of particular relevance to CO_2, is the need to correct for attenuation of intensities owing to atmospheric extinction at each Doppler-shifted line frequency. For CO_2 this is highly sensitive to Delta-dot, as seen from the order of magnitude improvement in our sensitivity estimates between -5 km s^{-1} (Fig. 14, top panel) and -10 km s^{-1} (Fig. 15, panel B).

Our formalism assumes spherically-symmetric gas outflow at constant speed (typically 0.8 km s^{-1} at 1 AU heliocentric distance) and incorporates photo-dissociation lifetime. Together these establish the fraction of all CO_2 molecules in the coma encompassed by the 5x5 $pixel^2$ (1.33x1.33 $arc\text{-}second^2$) beam (e.g., see Sections 2 and 3.1 in DiSanti et al. 2009). The corresponding mean column density within this “nucleus centered” aperture

(for Delta-dot = -10 km s^{-1}) is ~ 1.2 x 10^{13} CO_2 molecules cm^{-2}. The detection threshold for CO_2 improves substantially for larger values of Delta-dot (Fig. 15, panels C and D).

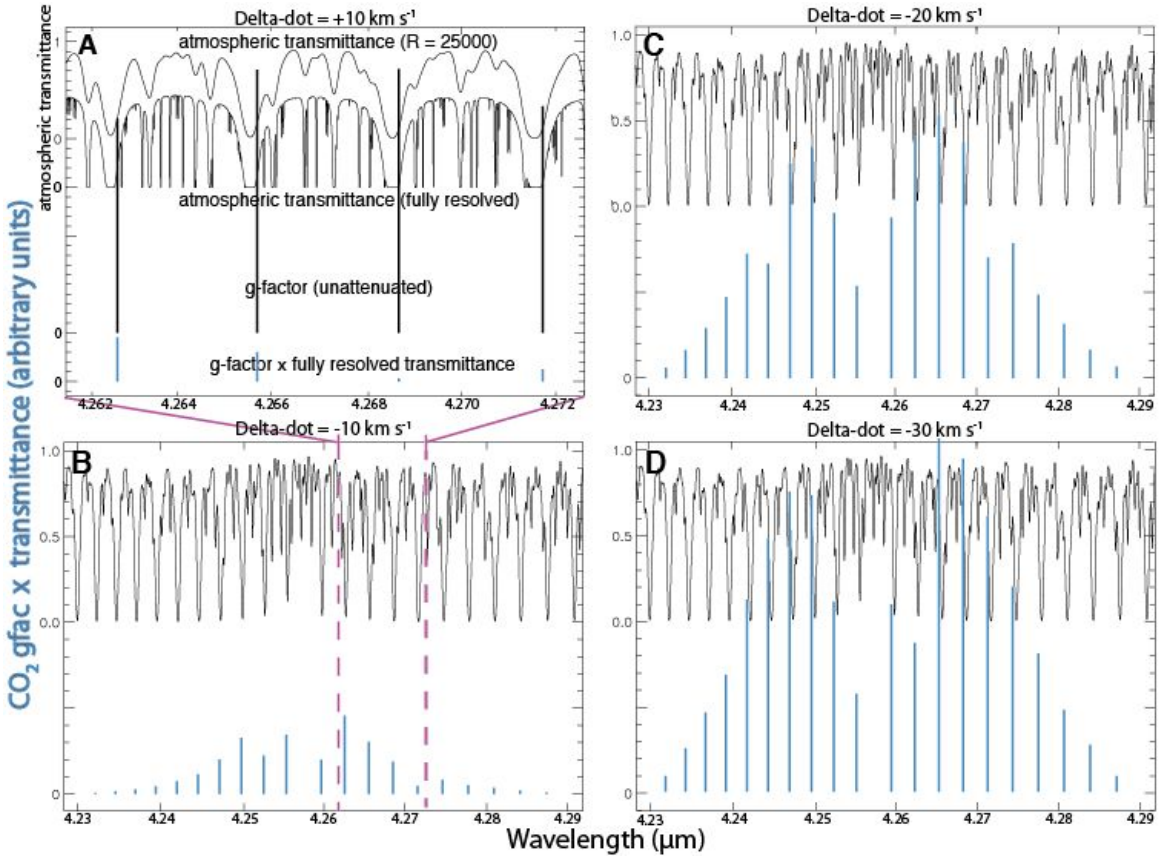

Figure 15. Prospects for detecting carbon dioxide v_3 emission from an altitude of 35 km for various geocentric Doppler shifts (Delta-dot values). The atmospheric transmittance function is shown in each panel for assumed air mass 1.5 and spectral resolving power R = 25000, as are stick spectra of transmitted line-by-line g-factors (shown in blue) at four values of Delta-dot. **A.** Fully resolved transmittance (R ~ 5 x 10^6) and unattenuated g-factors (Paganini et al., in prep.) are also shown. **B-D**. Transmitted CO_2 line intensities, illustrating the strong dependence of transmitted line flux on Delta-dot.

5.2.4.2 Methane (CH_4) and carbon monoxide (CO)

The "cometary organics" spectral region between ~ 3.2 and 3.6 μm is sampled efficiently using high-resolution (R ~ 20,000 or higher) ground-based spectroscopy. Principal species measured include C_2H_6, CH_3OH, CH_4, H_2CO, and OH prompt emission. Owing to telluric extinction, measuring lines in the v_3 band of CH_4 in particular from Mauna Kea (altitude 4.2 km) requires a geocentric Doppler shift of ±15 – 20 km s^{-1} or higher. However, this restriction is relaxed at GHAPS altitudes; even for zero geocentric velocity, transmittances in the strongest v_3 lines exceed 0.3, and for 5 - 10 km s^{-1} they are well above 0.9 (Fig. 16). This will especially benefit measuring CH_4 in comets near their closest approach to Earth (at which time Delta-dot passes through zero). It also expands the potential for sounding CH_4 in short-period comets, which are in general less

productive than Oort cloud comets. Short-period comets are underrepresented in IR compositional surveys, and their Delta-dot is frequently within 0 – 10 km s^{-1} when optimally placed for Earth-based observations. By similar reasoning, compared with ground-based observations, at small Delta-dot measurement of CO v_1 emission near 4.7 μm is much less affected by absorption from telluric CO. However, it is important to note that, given adequate Delta-dot, large ground-based telescope/instrument combinations (e.g., Keck/NIRSPEC) will outperform GHAPS' 1-m aperture for both CH_4 and CO, nonetheless GHAPS can fill a complementary role for small values of Delta-dot.

Owing to reduced telluric extinction, GHAPS can sense methane and carbon monoxide at much lower geocentric velocities compared to ground-based facilities.

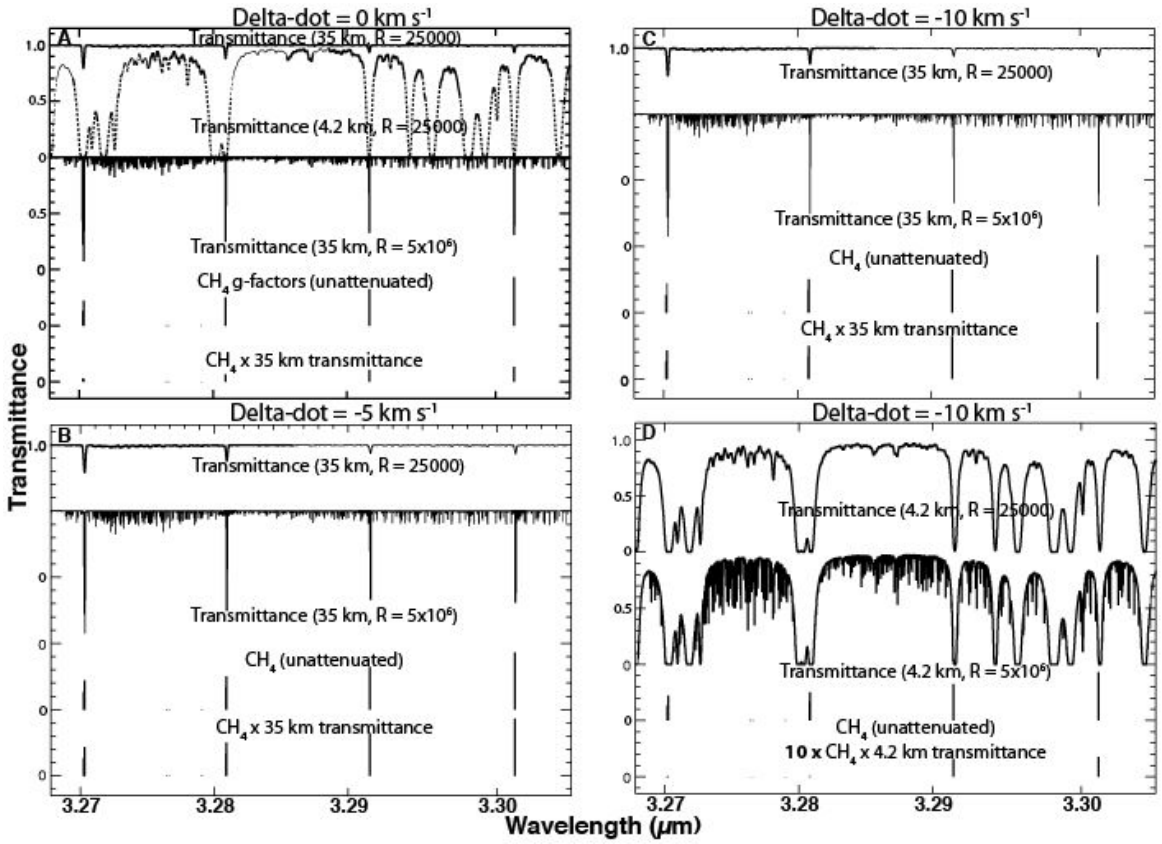

Figure 16. Prospects for measuring cometary CH_4 near 3.3 μm at small Doppler shifts (panels **A-C**). At 35 km, transmitted line intensities suffer minimal attenuation, even for very modest Delta-dot. **D**. Conversely, on Mauna Kea (4.2 km), even at Delta-dot = -10 km s^{-1} transmitted line intensities (bottom, shown multiplied by 10) are reduced to < 10% of their unattenuated levels.

5.2.4.3 Water (H_2O)

Figure 17 illustrates the prospects for detecting H_2O emission from comets and other solar system targets (e.g., plumes; § 5.2.5). Because GHAPS altitudes are above essentially all terrestrial water vapor, H_2O is detectable at arbitrary Delta-dot. For R =

20,000 – 25,000, and again assuming 1 AU heliocentric and geocentric distance we estimate a 10σ detection of line emission in the v_3 band of H_2O in 1 hour for a cometary water production rate of ~ 4 x 10^{26} molecules s^{-1}. Based on the same reasoning as applied previously to CO_2, this corresponds to a nucleus-centered column density of approximately 1.6 x 10^{13} water molecules cm^{-2}. Owing to its extremely low abundance in the terrestrial atmosphere at balloon altitudes, H_2O is also detectable at lower spectral resolving power, as was demonstrated by BOPPS through use of filter imaging (Cheng et al. 2016). However, higher resolution provides improved sensitivity and hence the ability to measure weaker comets.

Table 12. Requirements for measuring cometary H_2O, CO_2, CO, and CH_4.

Parameter	**Requirements**
Field of View	Long slit (> 10 arc-sec) (Ideal slit length 20-30 arc-sec) to allow for on-slit nodding
Filters/Wavelength Coverage	1 – 5 μm
Spectral Resolution	15,000 – 30,000
1D, 2D, or Multi-Object Spectroscopy?	1D, could include cross-dispersed echelle orders
Spatial Resolution	Diffraction limited
Guiding / Pointing Performance	100 mas (pointing), 200 mas (guiding)
Sensitivity/Associated SNR	~10^{-19} – 10^{-17} W m^{-2} *
Cadence/Duty Cycle/Total Experiment Duration	Minutes to hours (depending on cometary activity)
Subsystem Temperatures	Detector 30 K / OTA < 240 K

* 10σ in 1 hr. Detector read noise could become substantial below 3 μm.

Optical depth effects. For a comet with H_2O and CO_2 production rates near or above our estimated 10σ thresholds (~ a few x 10^{26} molecules s^{-1}), the stronger lines of these two molecules are expected to be optically thick, and to experience comparable degrees of optical depth. This is because although H_2O is the most abundant molecule in the cometary coma (at least within ~ 2 – 3 AU of the Sun), CO_2 lines are approximately a factor of 10 stronger due to the very large strength of its v_3 band, and this compensates for its lower abundance in comets (compared to H_2O). Thus v_3 lines of both H_2O and CO_2 could be optically thick. This should be considered, both when planning observations and also when interpreting spectra.

Tests for variability in production rates. In addition to individual measurements, GHAPS offers the potential for conducting time-resolved studies. These can search for variations in gas (and dust) production, both short-term (e.g., over a number of hours) and long-term (over days to weeks).

Short-term observations test changes associated with rotation of the nucleus, as was demonstrated most dramatically for Jupiter family comet 103P/Hartley-2 during its 2010 apparition. Gas production varied pronouncedly over an approximate 18-hour period (and multiples thereof, due to its non-principal-axis rotation) for weeks surrounding perihelion. Furthermore, CO_2 and H_2O were produced primarily from distinctly different regions on the nucleus, as demonstrated in great detail during the EPOXI flyby in November 2010 (A'Hearn et al. 2011).

Longer-term observations can be used to test for serial changes in gas production with heliocentric distance. A recent example of this is the long-period (Oort cloud) comet C/2009 P1 (Garradd), in which the abundance ratio CO/H_2O was a factor of four (or more) higher at 2 AU post-perihelion compared with 2 AU pre-perihelion (McKay et al 2015). A more recent study is of the dynamically new, Sun-grazing comet C/2012 S1 (ISON), which revealed dramatic increases in the abundance ratios of certain molecules (relative to H_2O) within 0.5 AU of the Sun (DiSanti et al. 2016). The potential for long-duration (e.g., up to ~ 100-day) GHAPS flights, particularly using super-pressure balloon technology, provides the potential for serial studies of future comets, with improved temporal coverage/cadence as well as more complete spectral coverage (e.g., including the direct measure of CO_2), compared with ground-based capabilities. Regarding cometary molecular composition, such studies are of paramount importance for addressing biases associated with measurements on only a single date, or on very few dates.

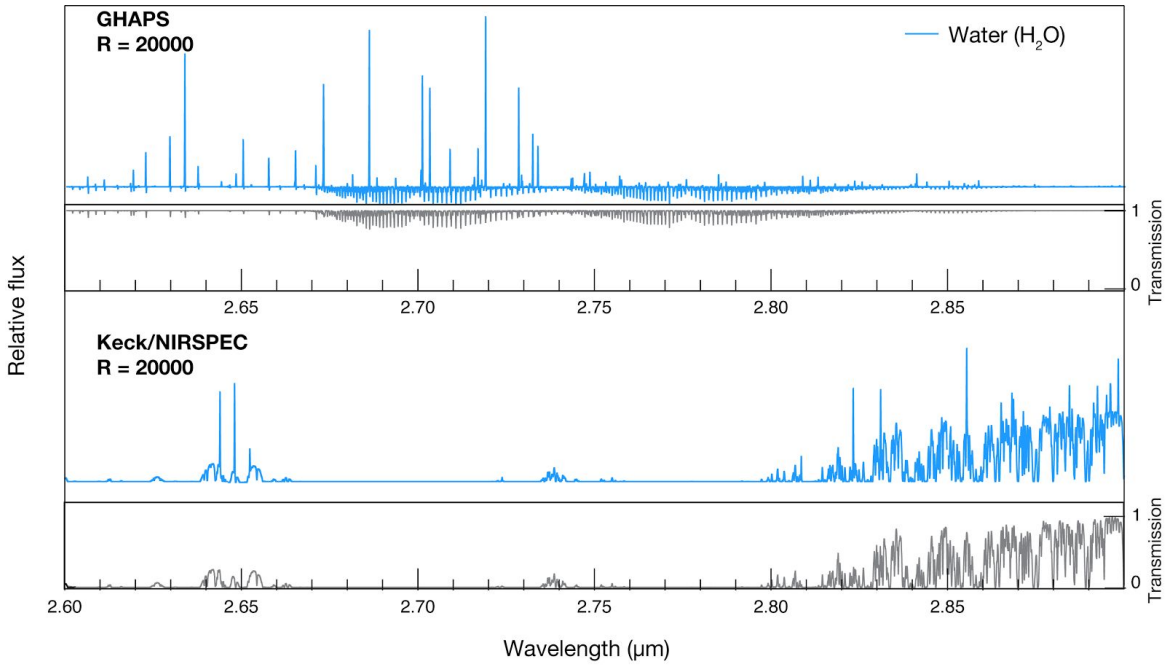

Figure 17. Detection of water by GHAPS vs. Keck/NIRSPEC. Infrared atmospheric transmittance at float altitude enables sensing H_2O in its strong v_3 fundamental band (at 2.73 μm), which is a factor of ~ 50 - 100 times stronger than hot-bands measured from ground-based facilities, but is not detectable from the ground due to extinction by the terrestrial atmosphere. Panels here are analogous to those for CO_2 in Fig. 14.

5.2.5 Water in plumes of icy ocean worlds

The existence of subsurface oceans in Europa and Enceladus satisfies a key requirement in our search for extraterrestrial life. While there are major uncertainties in how life began, our current understanding of its sustainability – as we know it – requires three basic conditions: liquid water, the availability of some key chemical elements generally in the form of accessible organic compounds (combinations of carbon, hydrogen, oxygen, nitrogen, phosphorus and sulfur), and a source of chemical energy (Spencer & Nimmo 2013; McKay et al. 2014, and references therein).

High-resolution spectroscopy on a balloon platform can provide unique molecular identification of water plumes in icy environments, offering clear advantages over ground based facilities (affected by significant terrestrial absorption).

High-resolution spectroscopy on a balloon platform can provide unique molecular identification of water plumes in icy environments within our solar system, and clear advantages over ground based facilities, which are affected by terrestrial extinction (see Fig. 17). For instance, a spectrograph with resolving power ($\lambda/\Delta\lambda$) > 10,000 can provide sensitivities of a few 10^{-19} W/m^2 (10$\boldsymbol{\sigma}$) for detection of water emission at 2.7 μm from an unresolved point source. For instance, first-order estimates indicate that GHAPS would be able to detect column densities of ~ 5 x 10^{14} water molecules cm^{-2} (10$\boldsymbol{\sigma}$), or ~1 x 10^{28} molecules s^{-1}, in a 4x5 pixel^2 aperture, or 1.1" (spatial) x 1.4" (spectral) assuming a pixel size of 0.27", which is suitable for targets with a 1" disk at 5 AU distance, such as Jovian moons. The formalism assumes spherically-symmetric gas outflow at constant speed of ~0.3 km/s at 5 AU heliocentric distance (based on observations of cometary lines, yet velocities in these environments could result in larger values) and incorporates water's photo-dissociation lifetime (above 500 hr at 5 AU).

The above column density corresponds to water outgassing of 300 kg s^{-1} (10$\boldsymbol{\sigma}$). As reference, the *HST* results for Europa's plumes indicated somewhat similar release parameters to those found in comets, namely water vapor content of ~10^{32} molecules (or 3 x 10^6 kg), ejection velocities of ~0.7 km/s and plume heights of ~200 km, which correspond to production rates on the order of ~2 x 10^{29} molecules s^{-1} (or 5000-7000 kg/s; Roth 2014). At Enceladus, *Cassini* flybys have returned somewhat lower values, such as ejection velocities of 0.4 km/s, plume heights of ~200–500 km and typical production rates on the order of ~1 x 10^{28} molecules/s (or 300 kg s^{-1}) (Hansen et al. 2006).

As in the case of cometary observations the high infrared transmittance of the atmosphere at float altitude enables sensing the key molecule H_2O through its strong v_3

band at 2.73 μm, not possible from the ground due to terrestrial extinction. As mentioned above, similar objectives were successfully achieved with the recent flight of BOPPS, which detected 2.73 μm water emission in comet Siding Spring, and measured the infrared water absorption feature on Ceres (Dankanich et al. 2016, Cheng et al. 2016).

Table 13. Requirements for measuring H_2O and organics in icy world plumes.

Parameter	Requirements
Field of View	Long slit (> 10") to allow nodding
Filters/Wavelength Coverage	2.5 – 5 μm
Spectral Resolution	> 5,000
1D, 2D, or Multi-Object Spectroscopy?	N/A
Spatial Resolution	Diffraction limited
Guiding / Pointing Performance	Sub-arcsecond
Sensitivity/Associated SNR	~10^{-19} W m^{-2} *
Cadence/Duty Cycle/Total Experiment Duration	Several minutes/hours
Subsystem Temperatures	Detector at 30 K / OTA < 240 K

* 10σ in 1 hr (R = 10,000). Detector read noise could become substantial below 3 μm.

5.3. Thermal IR (TIR)

5.3.1 Heterogeneity of the Lunar Mantle

The Moon is an extended object, and most of its illuminated surface is warmer, or much warmer than the GHAPS telescope, so observations will be object signal limited. GHAPS allows access to the 10–30 μm region and enables unique compositional measurements. The titanium oxide ilmenite is the fourth most abundant mineral on the Moon, but remote measurements of its abundance and distribution are highly uncertain (Gillis-Davis et al. 2006). Estimates of titanium contents from ultraviolet and visible spectral reflectance and neutron spectroscopy are in stark disagreement and the discrepancy is unexplained. In the 10–30 μm region oxides like ilmenite show strong spectral features (Fig. 18) as shown by spectra of particular ilmenite extracted from lunar rocks (Isaacson et al. 2011), so GHAPS measurements would contribute uniquely to this problem. While the diffraction limited resolution of GHAPS at 30 μm would be about 30 km, this is higher than the resolution of the neutron measurements that reveal the shortcomings in UV-Vis estimates of titanium and is sufficient to resolve major lunar features and geologic units.

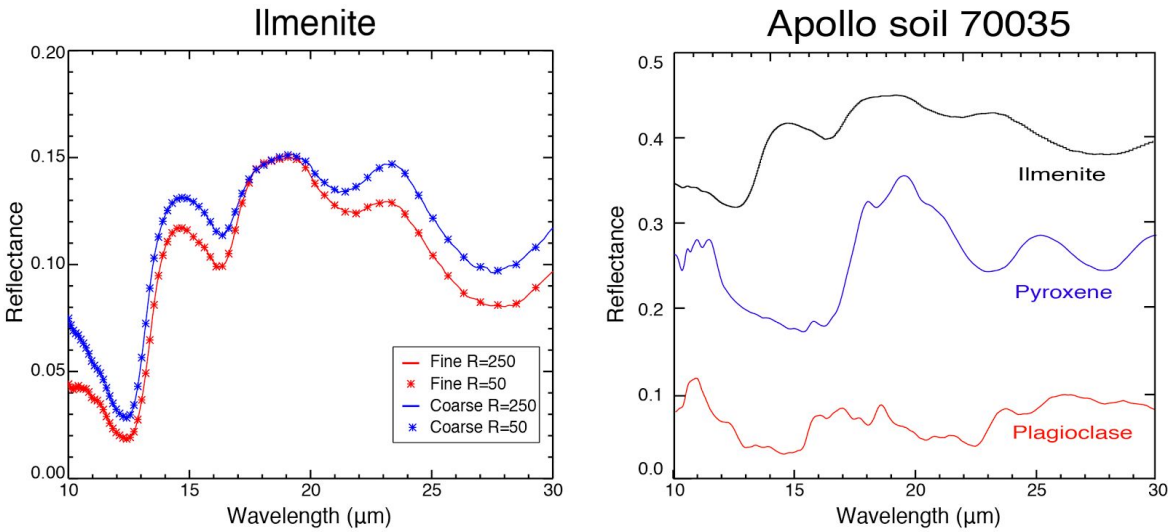

Figure 18: Ilmenite, Pryoxene and Plagioclase extracted from lunar sample 70035 from the Apollo 17 site. On left the particulate samples were crushed into standard grain sizes, coarse grained and < 45 µm. Original data with a spectral resolution of R = 250 is plotted with a solid line, data resampled to an R = 50 is plotted with asterisks. The right image compares common lunar minerals with Ilmenite. To distinguish the spectra, 0.15 and 0.3 was added to the reflectance for Pyroxene and Ilmenite respectively. http://www.planetary.brown.edu/LRMCC/

Table 14. Measurement requirements for lunar mantle science case.

Parameter	Requirements
Field of View	10” (IFOV)
Filters/Wavelength Coverage	10 - 30 µm
Spectral Resolution	50
1D, 2D, or Multi-Object Spectroscopy?	1D Spectroscopy
Spatial Resolution	20 km
Guiding / Pointing Performance[1]	3”
Sensitivity/Associated SNR	SNR > 100
Cadence/Duty Cycle/Total Experiment Duration	< 1 min
Subsystem Temperatures	Ambient

[1]Guiding based on keeping large lunar features on the slit.

5.3.2 Volatiles on Mercury

Mercury is the least-studied terrestrial planet having limited Earth observations and only two spacecraft visits, by Mariner 10 and MESSENGER. While Mercury at maximum elongation only subtends 5-10 arcseconds, and so would be unresolved above about 10 – 20 μm from the GHAPS platform, there are compositional questions for Mercury that are addressable at the hemispheric scale (and clearly its high surface temperatures would ensure abundant signal). Mercury is typically observed from the Earth before sunrise at high airmass and is greatly affected by atmospheric turbulence. Observations of Mercury will likely need to be made before sunrise, to avoid heating the telescope and baffles. The same processes invoked for global lunar water should in principle operate on Mercury, that is, solar wind protons interact with oxygen in surface minerals to produce water (Zeller et al. 1966). While the presence of water on the Moon was surprising, that discovery suggests that similar water may be present, and possibly detectable, on Mercury.

A small number of observations of Mercury in the thermal infrared in the 8 – 14 μm window have been reported (e.g Sprague et al. 1994). BepiColombo, if successful, carries a spectrometer (MERTIS) that operates from 7 – 14 μm to measure silicate spectral features. Sulfides and possibly oxides are also a likely surface constituent of the surface of Mercury (Nittler et al. 2011), and GHAPS, depending on its ability to look within 20 degrees of the sun, could provide observations in the 10 – 30 μm region providing definitive detection of these surface minerals (e.g. Keller et al. 2002). Neither MESSENGER nor the planned BepiColombo missions carried or will carry instruments sensitive in these critical wavelength regions, thus spectral evidence of oxides that may be present on Mercury's surface are available to a suitable high altitude observatory. Observations at 20 μm enables detection of hematite on Mars at a 10% level by weight with a signal-to-noise of ~400. While FORCAST on board SOFIA observes in the 5 - 40 μm region, SOFIA could point within 20 degrees of the Sun (Gehrz et al. 2011) however Mercury would only be observable for a short time while looking through most of the atmosphere. From GHAPS Mercury would be available to observe for a longer time while also looking through less atmosphere due to the float altitude of GHAPS.

Table 15. Measurement requirements for Mercury volatiles science case.

Parameter	**Requirements**
Field of View	10” (IFOV)
Filters/Wavelength Coverage (μm)	10 - 30 μm
Spectral Resolution[1]	50
1D, 2D, or Multi-Object Spectroscopy?	2D Spectroscopy
Spatial Resolution	Hemisphere
Guiding / Pointing Performance	3”
Sensitivity/Associated SNR	SNR > 400

Cadence/Duty Cycle/Total Experiment Duration	< 1 min
Subsystem Temperatures	Ambient

[1]An R = 50 is sufficient to resolve oxides on the Lunar surface so it is assumed that similar oxides on Mercury will be resolvable at an R = 50 (Fig. 18).

6. General Purpose vs. Spectrally Optimized Flights

Much like a space mission, each flight of GHAPS must commit to a specific instrument/optical configuration for the duration of a flight. The most versatile configuration would accommodate broad wavelength coverage from the UV to mid-IR and switching between instrumental capability spanning broadband imaging to high-resolution spectroscopy. Although such versatility is attractive, it may not be practical to implement and will certainly involve performance compromises. As a simple concrete example, gold mirror coatings would best optimize system emissivity and thus thermal infrared sensitivity. Such coatings, however, would render the system blind to the ultraviolet. This study recommends that each GHAPS flight be optimized for a more narrow range of capabilities. A clear dividing line lies between the UV/Visible/near-infrared (0.2 – 2.5 μm) and wavelengths > 2.5 μm where telescope thermal emission (Poisson noise) could dominate sensitivity. Several specific drivers for optimization are discussed below.

6.1. Image Scale

GHAPS will be near diffraction limited across its operating wavelength range. The image size will vary by more than an order of magnitude from the near-UV (0.1”) to the thermal infrared (3” at 10 μm). The 14 meter native focal length of the GHAPS telescope will produce a pixel scale of 0.15”/pixel. Pixels that are 10 μm in size thus will be well matched to the 0.55” FWHM of the diffraction-limited point spread function at 2.2 μm. To avoid undersampling at shorter wavelengths, optics are required to increase the focal length several times. These differing requirements drive the telescope design in different directions depending on the short vs. long wavelength trade, or require insertable reimaging optics for the short wavelength science.

The varying image size directly constrains system performance in two additional ways. First, to achieve diffraction limited image quality each optical surface must be figured to better than λ/40 accuracy. Infrared requirements on mirror surface accuracy at 5000 nm are thus 10 times less restrictive than at 500 nm. Optics fashioned to meet the UV requirements will certainly serve diffraction limited IR imaging well. On the other hand, given the relaxed figure requirements, an IR focused mission could be designed around a less expensive, and more importantly, less massive primary mirror. Given the expected

large mass of cryostat-enclosed infrared instruments, reduced weight may be a significant advantage.

Second, telescope pointing stability requirements scale directly with angular subtense of the target. At near-UV wavelengths the focal plane stability requirement might be as small as 30 milliarcseconds RMS to maintain 0.1" image quality, whereas an infrared-only configuration might require pointing only at the level of 250 milliarcseconds to maintain 0.75" diffraction limited image quality. Difficulty and complexity of maintaining balloon platform pointing stability scales nonlinearly with increasingly precise requirements. An infrared-only mission would require only minor refinement of the 1-arcsecond RMS pointing delivered by the WASP platform, and improvements in WASP pointing may enable an infrared optimized system to operate with native WASP pointing.

6.2. System Emissivity and Thermal Infrared Sensitivity

Given the high infrared transmission of the sky at balloon altitude, telescope emission dominates system sensitivity with the exception of a few high opacity spectral regions arising from well-mixed CO_2 and residual water vapor (Fig. 6). Thermal emission from the telescope optics dominates system noise at wavelengths longward of ~ 2.5 μm for broadband measurements for mirror temperatures > 200 K. There are four direct ways to minimize the thermal Poisson noise: (1) minimize the emissivity of each warm optical component (alternatively, maximize its reflectivity), (2) minimize the number of warm optical components between the sky and the cryogenic instrument optics, (3) cleanly cold-baffle the system with a masked pupil image in the cold volume of the infrared instrument, masking the central hole image and secondary supports, and, (4) minimize the telescope temperature. However, some items in this list are at odds with the optimal design for a UV/visible system.

As discussed above, the optimal infrared coating is protected gold, which has ~99% reflectivity (1% emissivity across the thermal infrared region). Compromise coatings still have excellent performance (95 - 98% reflectivity), but this excellent reflectivity at least doubles the emissivity per surface and, depending on the coating, can increase emissivity several times.

The ideal infrared imaging or spectroscopic system will have only three components before the cold interior surfaces of the cryostat: the telescope primary, the secondary mirror, and the instrument window. With optimized gold coatings on the mirrors and a well-designed broadband dielectric anti-reflection coating on the cryostat window, the total system emissivity can be as low as 3% (presuming near perfect masking of the telescope warm surfaces at the reimaged telescope system pupil). Given the need for fine steering of the image at the arcsecond level, an articulated secondary mirror can alleviate the need for separate warm beam steering optics. This assumes that there is a means of precisely detecting pointing offsets without adding system emissivity, for example by using a window mode on H2RG devices. A shared infrared/optical configuration would require, at minimum, a gold coated insertable pickoff mirror to switch between long focal

length visible imaging and infrared science, and possibly might have to share other emitting optical elements with the visible system.

Finally, the temperature of the warm optical components can have a tremendous impact on infrared sensitivity, particularly at wavelengths on the blue side of the Wien peak of the ambient blackbody distribution. For ground-based telescopes at ~280 K, thermal radiation becomes the dominant source of noise at wavelengths longward of 2.2 μm. Lowering the telescope optics temperature to ~200 K via radiative cooling at float altitude will substantially reduce the near-infrared background, improving sensitivities between 2.5 - 4 μm by up to 2-3 stellar magnitudes (Appendix 3). Such sensitivities for the 1-m GHAPS telescope are equivalent to 3-5 meter class telescope sensitivities on the ground in this infrared regime. However, this advantage degrades quickly with increasing telescope temperature. In this case the advantage goes to the UV/Visible system, which has thermal uniformity and stability constraints but no strong radiative cooling requirement. The infrared optimized mission will require well designed Earth and Sun shades and OTA construction that can support near-cryogenic temperatures. In contrast, significant radiative cooling of the primary mirror could compromise the image quality for UV/Vis observations in a combined mission. **The substantial difference in thermal requirements between the UV/Vis and IR configurations argues strongly for separately optimized missions.**

6.3. Instrument Cryogenic and Power Requirements

Cooling and power requirements can differ significantly between the UV/Visible (CCD based) spectral region and infrared wavelengths, where HgCdTe detectors are typically used. Visible imaging instrument volumes can be compact, with only modest cooling power required to maintain a detector temperature of ~140 K needed to minimize dark current. Infrared arrays sensitive out to 5.2 μm require cooling to < 60 K to perform optimally. Infrared instrument volumes also tend to be larger to accommodate cold pupil re-imaging as well as cooling all system optical elements.

For short (< 2 day) balloon flights, classical liquid cryogens – nitrogen in particular – can provide the necessary instrument cooling. One Watt of cryogenic cooling consumes 0.5 liters of liquid nitrogen in a day. Thus, an instrument requiring 15 liters/day (30 W cooling power) would require more than 2000 liters (1600 kilograms) for a 100-day mission when storage loss is accounted for. Liquid cryogen volumes for a long duration (> 50 day) flight would thus be prohibitive, pushing designs toward closed cycle coolers and their associated power requirements.

The warmer temperatures and lower dissipated cold wattage associated with the UV/Visible detector cooling requirements suggest a more modest power consumption for a UV/Visible system. A simple Joule-Thompson cooling system with a sustained input power of order 250 W can provide a heat lift at 77 K of 15 W, which is sufficient for a small cryostat and a detector operating at 140 K. The thermal mass connected to such a cooler – particularly the CCD/CMOS array – would be small and cooldown times would be short, so this cooler could operate as needed.

Cryocoolers become less efficient at lower temperatures and cooling below 60 K, as would be required for low dark current operation of a 5.2 μm HgCdTe device, may require use of a less efficient pulse tube technology. Input power requirements to cooling systems are of order 15 – 40 W for each Watt of cold dissipated power with the higher input wattages required at the lowest temperatures. The overall power dedicated to cooling will scale with the heat load on the cryostat, with 20–50 W being typical of modest scale infrared instruments. Roughly a kilowatt of continuous input power might be necessary to cool a large infrared system. Cooling times to reach equilibrium for such instruments can be greater than a day, so continuous cooling over the multiple days that would be needed for a sustained observing campaign would require daily power consumption/generation of 24 kWh. To sustain this level of power, solar panels with peak full-sun capacity of roughly 3–4 kW will need to be coupled to batteries with a storage capacity of at least 20 kWh, providing 15 kWH of nighttime capacity with 30% margin. Efficient lithium ion batteries can store power at the level of 0.25 kWh/kg, implying a battery mass of 100 kg to provide the needed capacity.

In summary, the considerations of image scale, system emissivity, power, and cooling reveal substantially different requirements for UV/Vis versus infrared instruments on a balloon-borne platform. This argues for spectrally optimized flights of GHAPS that are designed to take advantage of particular wavelength regimes and the associated instrument and telescope design features.

7. References

A'Hearn, M. F.; M. J. S. Belton; W. A. Delamere; L. M. Feaga; D. Hampton; et al. (2011). EPOXI at Comet Hartley 2, Science, 332, 1396-1400, doi:10.1126/science.1204054

Barthol, P.; A. Gandorfer; S. K. Solanki; M. Schussler; B. Chares; et al. (2011). The Sunrise Mission, Solar Phys 268, 1-34, doi: 10.1007/s11207-010-9662-9

Berthier, J.; F. Vachier; F. Marchis; J. Durech; B. Carry (2014). Physical and dynamical properties of the main belt triple Asteroid (87) Sylvia, Icarus, 239, 118-130, doi: 10.1016/j.icarus.2014.05.046

Cheng, A. F.; C. Hibbitts; E. F. Young; P. N. Bernasconi; K. Tibor; et al. (2014). BOPPS Observations of Oort Cloud Comets Siding and PanSTARRS, American Geophysical Union, Fall Meeting 2014, abstract #P42A-04

Cheng, A. F.; C. A. Hibbitts; R. Espiritu; R. McMichael; Z. Fletcher; et al.(2016). Stratospheric balloon observations of Comets C/2013 A1 (Siding Spring), C/2014 E2 (Jacques), and Ceres, Icarus (in press).

Clark, R. N. (2009). Detection of adsorbed water and hydroxyl on the Moon, Science 326, 562–564, doi: 10.1126/science.1178105.

Clough, S. A.; M. W. Shephard; E. J. Mlawer; J. S. Delamere; et al. (2005). Atmospheric radiative transfer modeling: a summary of the AER codes, JQSRT, 91, 233-244, doi: 10.1016/j.jqsrt.2004.05.058

Dankanich, J. W.; T. Kremic; K. Hibbitts; E. F. Young; R. Landis (2016). Planetary Balloon-Based Science Platform Evaluation and Program Implementation: Final Report. NASA/TM-2016-218870.

Denny, S. P.; J. Y. Yuen; P. M. Lubin (2013). The fundamental limits of detection in the far infrared, New Astronomy, 25, 114-129, doi: 10.1016/j.newast.2013.04.008 https://arxiv.org/pdf/1401.1604.pdf

DeSanctis, M. C., et al. (2015). Ammoniated phyllosilicates with a likely outer Solar System origin on (1) Ceres, Nature (letters), doi:10.1038/nature16172

DiSanti, M. A.; G. L. Villanueva; S. N. Milam; L. N. Zack; B. P. Bonev, et al. (2009). A multi-wavelength study of parent volatile abundances in Comet C/2006 M4 (SWAN), Icarus, 203, 589-598, doi: 10.1016/j.icarus.2009.05.026

DiSanti, M. A.; B. P. Bonev; E. L. Gibb; L. Paganini; G. L. Villanueva, et al. (2016). En route to destruction: the evolution in composition of ices in comet D/2012 S1 (ISON) between 1.2 and 0.34 AU from the Sun as revealed at infrared wavelengths, ApJ 820, 34 (20pp), doi:10.3847/0004-637X/820/1/34

Esposito, L. W., J.-L. Bertaux; V. A. Krasnopolsky; V. I. Moroz; L. V. Zasova (1997). Chemistry of lower atmosphere and clouds. In: *Venus II*. University of Arizona Press, Tucson, AZ, pp. 415–458.

Feaga, L. M.; M. F. A'Hearn; J. M. Sunshine; O. Groussin; T. L. Farnham (2007). Asymmetries in the distribution of H_2O and CO_2 in the inner coma of Comet 9P/Tempel 1 as observed by Deep Impact, Icarus, 190 (2), 345-356, doi: 10.1016/j.icarus.2007.04.009

Feaga, L. M.; M. F. A'Hearn; T. L. Farnham; D. Bodewits; J. M. Sunshine; et al. (2014). Uncorrelated volatile behavior during the 2011 apparition of comet C/2009 P1 (Garradd), AJ, 147, 24-37, doi: 10.1088/0004-6256/147/1/24

Ford, H. C.; L. D. Petro; C. Burrows; C. Ftaclas; M. C. Roggemann; J. T. Trauger (2002). Artemis: a stratospheric planet finder, Adv. Space Res., 30, 1283-1288, doi:10.1016/S0273-1177(02)00544-6

Giavalisco, M.; K. Sahu; R. C. Bohlin (2002). New estimates of the sky background for the HST Exposure Time Calculator, STScI Instrument Science Report WFC3 2002-12 (9 pp.)

Gehrz, R. D.; E. E. Becklin; J. De Buizer; T. Herter; L. D. Keller; et al. (2011). Status of the Stratospheric Observatory for Infrared Astronomy (SOFIA), *Adv. Sp. Res.,* 48 (6), 1004-1016, doi: 10.1016/j.asr.2011.05.023

Gillis-Davis, J. J.; P. G. Lucey; B. R. Hawke (2006). Testing the relation between UV–VIS color and TiO2 content of the lunar maria, *Geochimica et cosmochimica acta,* 70, 24, 6079-6102, doi: 10.1016/j.gca.2006.08.035

Hansen, K. C.; K. Khurana; D. L. de Zeeuw (2006). Rotational driving of Jupiter's magnetosphere and current sheet, American Geophysical Union, Fall Meeting 2006, abstract #SM21E-03

Hendrix, A. R.; K. D. Retherford; R. G. Gladstone; D. M. Hurley; P. D. Feldman; et al. (2012). The lunar far-UV albedo: Indicator of hydration and weathering, J. Geophys. Res., 117, E12, E12001, doi:10.1029/2012JE004252

Hibbitts, C. A.; G. A. Grieves; M. J. Poston; M. D. Dyar; A. B, Alexandrov; et al. (2011). Thermal stability of water and hydroxyl on the surface of the Moon from temperature-programmed desorption measurements of lunar analog materials, Icarus, 213, 64-72, doi:10.1016/j.icarus/2011.02.015

Isaacson, P. J.; A. Basu Sarbadhikari; C. M. Pieters; R. L. Klima; T. Hiroi; Y. Liu; L. A. Taylor (2011). The lunar rock and mineral characterization consortium: Deconstruction and integrated mineralogical, petrologic, and spectroscopic analyses of mare basalts, Meteorit. Planet. Sci., 46, 228-251, doi:10.1111/j.1945-5100.2010.01148.x

Kanuchova, Z.; R. Brunetto; D. Fulvio; G. Strazzulla (2015). Near-ultraviolet bluing after space weathering of silicates and meteorites, Icarus, 258, 289-296, doi: 10.1016/j.icarus.2015.06.030

Karkoschka, E. (2011). Neptune's cloud and haze variations 1994-2008 fro 500 HST-WFPC2 images. Icarus 215, 759-773, doi:10.1016/j.icarus.2011.06.010

Keane, J. T.; I. Matsuyama (2014). Hill slope failure as a mechanism to resurface asteroids during planetary flybys, Lunar and Planetary Science Conference, 45, 2733 (Contribution #1777)

Keller, L. P.; S. Hony; J. P. Bradley; F. J. Molster; L. B. F. M. Waters; et al. (2002). Identification of iron sulphide grains in protoplanetary disks, Nature, 417, 148-150, doi:10.1038/417148a

Kern, S. D.; J. L. Elliot (2006). Discovery and characteristics of the Kuiper belt binary 2003QY90, Icarus, 183, 179-185, doi:10.1016/j.icarus.2006.01.002

Khatuntsev, I. V.; M. V. Patsaeva; D. V. Titov; N. I. Ignatiev; A. V. Turin; et al. (2013). Cloud level winds from the Venus Express Monitoring Camera imaging, Icarus, 226, 140-150, doi:10.1016/j.icarus.2013.05.018

Leinart, Ch., et al. (1998). The 1997 reference of diffuse night sky brightness, A&ASS, 127, 1-99

Limaye, S. S.; C. Grassotti; M. J. Kuetemeyer (1988). Venus: cloud level circulation during 1982 as determined from the Pioneer cloud photopolarimeter images. I. Time and zonally averaged circulation, Icarus, 73, 193–211, doi: 10.1016/0019-1035(88)90093-0

Livengood, T. A.; G. Chin; R. Z. Sagdeev; I. G. Mitrofanov; W. V. Boynton; Evans, L. G.; et al. (2015). Moonshine: Diurnally varying hydration through natural distillation on the Moon, detected by the Lunar Exploration Neutron Detector (LEND), Icarus, 255, 100–115, doi: 10.1016/j.icarus.2015.04.004

Livengood, T. A.; L. D. Deming; M. F. A'Hearn; D. Charbonneau; T. Hewagama; et al. (2011). Properties of an Earth-Like planet orbiting a Sun-like star: Earth observed by the EPOXI Mission, Astrobiology, 11, 907–930, doi: 10.1089/ast.2011.0614

Males, J. R.; L. M. Close; O. Guyon, K. M. Morzinski; et al. (2016). The path to visible extreme adaptive optics with MagAO-2K and MagAO-X. Proc. SPIE 9909, *Adaptive Optics Systems V*, 990952, doi:10.1117/12.2234105.

Marcq, E.; D. Belyaev; F. Montmessin; A. Feorova; et al. (2011). An investigation of the SO_2 content of the venusian mesosphere using SPICAV-UV in nadir mode, Icarus, 211, 58-69, doi: 10.1016/j.icarus.2010.08.021

Marcq, E.; J.-L. Bertaux; F. Montmessin; and D. Belyaev (2013). Variations of sulphur dioxide at the cloud top of Venus's dynamic atmosphere. Nature Geoscience 6, 25-28, doi:10.1038/ngeo1650.

Markiewicz, W.J.; D. V. Titov; S. S. Limaye; H. U. Keller; N. Ignatiev; et al. (2007). Morphology and dynamics of the upper cloud layer of Venus, Nature, 450 (7170), 633–636, doi: 10.0138/nature06320

Markiewicz, W. J.; E. Petrova; O. Shalygina; M. Almeida; D. V. Titov; et al. (2014). Glory on Venus cloud tops and the unknown UV absorber, Icarus, 234, 200-203, doi:10.1016/j.icarus.2014.01.030

McCord, T. B.; J.-Y. Li; J.-P. Combe; H. Y. McSween; R. Jaumann; et al. (2012). Dark material on Vesta from the infall of carbonaceous volatile-rich material, Nature, 491 (7422), 83-86, doi:10.1038/nature11561

McCord, T. B.; J. Combe (2010). Analysis of the behavior of the 3 μm absorptions in the M3 lunar reflectance observations and indications of OH sources and processes for airless bodies., AGU Fall Meeting, Abstract #P13E-01
(http://adsabs.harvard.edu/abs/2010AGUFM.P13E..01M)

McKay, C.P., Anbar, A.D., Porco, C., Tsou, P. (2014). Follow the Plume: The Habitability of Enceladus Astrobiology, 14, 352-355

McKay, A. J.; A. L. Cochran; M. A. DiSanti; G. Villanueva; N. Dello Russo; et al. (2015). Evolution of H_2O, CO, and CO_2 production in Comet C/2009 P1 (Garradd) during the 2011-2012 apparition, Icarus, 250, 504-515, doi: 10.1016/j.icarus.2014.12.023

National Research Council (NRC) Committee on the Planetary Science Decadal Survey (2011). *Vision and Voyages for Planetary Science in the Decade 2013-2022*. National Academies Press, National Academy of Science, Washington, DC.
Nesvorny, D.; A. N. Youdin; D. C. Richardson (2010), formation of Kuiper Belt binaries by gravitational collapse, AJ, 140, 785-793, doi: 10.1088/0004-6256/140/3/785

Nittler, L. R.; R. D. Starr; S. Z. Weider; T. J. McCoy; W. V. Boynton; et al (2011). The major-element composition of Mercury's surface from MESSENGER x-ray spectrometry, Science, 333 (6051), 1847-1850, doi:10.1126/science.1211567

Ootsubo, T.; H. Kawakita; S. Hamada; H. Kobayashi; M. Yamaguchi; et al. (2012). AKARI near-infrared spectroscopic survey for CO_2 in 18 comets, ApJ, 752, 15-26, doi:10.1088/0004/637X/752/1/15

Paganini, L.; M. J. Mumma; G. L. Villanueva; J. V. Keane; G. A. Blake; B. P. Bonev; et al. (2014). C/2013 R1 (Lovejoy) at IR wavelengths and the variability of CO abundances among Oort cloud comets, ApJ, 791(2), 122-129, doi: 10.1088/0004-637X/791/2/122

Parker, A. H.; J. J. Kavelaars; J.-M. Petit; L. Jones; B. Gladman; J. Parker (2011). Characterization of seven ultra-wide trans-Neptunian binaries, ApJ, 743, 1-20, doi: 10.1088/0004-637X/743/1/1

Parker, A. H.; J. J. Kavelaars (2012). Collisional evolution of ultra-wide trans-Neptunian binaries, ApJ, 744, 139-152, doi: 10.1088/0004-637X/744/2/139

Parker, A. H.; M. W. Buie; W. M. Grundy; K. S. Noll (2016). Discovery of a Makemakean moon, ApJL, 825-829, L9, doi: 10.3847/2041-8205/825/1/L9

Peralta, J.; R. Hueso; A. Sanchez-Lavega (2007). A reanalysis of Venus winds at two cloud levels from Galileo SSI images, Icarus, 190, 469-477, doi:10.1016/j.icarus.2007.03.028

Petrova, E. V.; O. S. Shalygina; W. J. Markiewicz (2015). The VMC/VEx photometry at small phase angles: Glory and the physical properties of particles in the upper cloud layer of Venus, Planet. Sp. Sci., 113, 120-134, doi:10.1016/j.pss.2014.11.013

Poston, M. J.; G. A. Grieves; A. B. Aleksandrov; C. A. Hibbitts; D. M. Dyar; T. M. Orlando (2013). Water interactions with micronized lunar surrogates JSC-1A and albite under ultra-high vacuum with application to lunar observations, J. Geophys. Res., 118, 105-115, doi:0.1029/2012JE004283

Richardson, D. C.; W. F. Bottke; S. G. Love (1998). Tidal distortion and disruption of Earth-crossing asteroids, Icarus, 134, 47-76, 10.1006/icar.1998.5954

Rivkin, A. S.; E. L. Volquardsen; B. E. Clark (2006). The surface composition of Ceres: Discovery of carbonates and iron-rich clays, Icarus, 185, 563-567, doi:10.1016/j.icarus.2006.08.022.

Robert, C.; J.-M. Conan; V. Michau; J.-B. Renard; C. Robert; F. Dalaudier (2008). Retrieving parameters of the anisotropic refractive index fluctuations spectrum in the stratosphere from balloon-borne observations of stellar scintillation, J. Opt. Soc. Am. A, 25 (2), 379-393, doi: 10.1364/JOSAA.25.000379

Roth, L.; J. Saur; K. D. Retherford; D. F. Strobel; P. D. Feldman; et al. (2014). Transient water vapor at Europa's south pole, *Science*, 343 (6167), 171-174, doi: 10.1126/science.1247051

Schlichting, H. E.; R. Sari (2008). Formation of Kuiper Belt binaries, ApJ, 673 (2), 1218-1224, doi: 10.1086/524930

Simons, D. (2015). Current Status & Future PLans at CFHT. Presentation at Subaru Users Meeting, Jan. 2015. http://subarutelescope.org/Projects/subaru_um2014/presentation/jan14am/03_doug_simons_um2014.pdf

Sprague, A. L.; R. W. H. Kozlowski; F. C. Witteborn; D. P. Cruikshank; D. H. Wooden (1994). Mercury: Evidence for anorthosite and basalt from mid-infrared (7.3-13.5 micrometers) spectroscopy, Icarus, 109, 156-167, doi:10.1006/icar.1994.1083

Sunshine, J. M.; T. L. Farnham; L. M. Feaga; O. Groussin; F. Merlin; R. E. Milliken; M. F. A'Hearn (2009). Temporal and spatial variability of lunar hydration as observed by the Deep Impact spacecraft, Science, 326, 565–568, doi: 10.1126/science.1179788

Tsang, C. C. C.; J. R. Spencer; K. L. Jessup (2013). Synergistic observations of Io's atmosphere in 2010 from HST-COS in the mid-ultraviolet and IRTF-TEXES in the mid-infrared, Icarus, 226, 604-616, doi:10.1016/j.icarus.2013.06.010

Zeller, E. J.; L. B. Ronca; P. W. Levy (1966). Proton-induced hydroxyl formation on the lunar surface, J. of Geophys. Res., 71, 4855-4860, doi: 10.1029/JZ071i020p04855

Zombeck, M. V. (1990). Handbook of Space Astronomy and Astrophysics, 2nd edition. Cambridge, UK: Cambridge University Press: http://ads.harvard.edu/books/hsaa/index.html

Appendix 1: Master list of instrument requirements for science cases in Section 5.

Table A.1 on the subsequent page contains a summary listing of the GHAPS instrument requirements for all of the science cases examined in §5 and listed in Tables 4 - 15. This information was used to identify commonalities as well as key drivers for a suite of instrumentation capable of addressing the broadest possible range of planetary science measurement objectives from a balloon-borne platform.

A higher resolution version of Table A.1 is located here:
https://docs.google.com/spreadsheets/d/1onBHmXZsxhAmqJ1aJU-eGQ-Xa-kguti8G86cGcBAVUg/edit?usp=sharing

Table A1. GHAPS Instrument Requirements Table

Parameter	minor planet binaries	venus wind tracking	giant planet cloud tracking	asteroid space weathering	Ionian and Venusian volcanoes via atmospheric SO2	Jovian aurorae	variability of Lunar water	asteroid organics and volatiles	volatiles in comets	Water/organics in plumes	lunar mantle	mercury volatiles
Section Number	**5.1.1**	**5.1.2**	**5.1.3**	**5.1.4**	**5.1.5**	**5.2.1**	**5.2.2**	**5.2.3**	**5.2.4**	**5.2.5**	**5.3.1**	**5.3.2**
Field of View	~180"	1 arcmin or greater	1 arcmin	~180"	Io: Several arcseconds Venus: 1 arcmin or greater	1 arc minute (Jupiter is ~43 arcsec diameter)	~3 arc minute (for image mosaicking)	> 10 arc-sec to allow nodding	Long slit (> 10 arc-sec) to allow nodding	Long slit (> 10") to allow nodding	10" (IFOV)	10" (IFOV)
Filters/Wavelength Coverage (μm)	Medium- to Broad-band optical (Johnson- or SDSS-like.)	near-UV (250-400 nm)	UV-Vis narrowband (specific filters to match HST/WFPC2)	200 nm to 800 nm Space weathering: Narrowband (10-50nm) Structural changes: Medium- to Broad-band optical	UV: 210-235 nm; 270-320 nm	3.4 μm ± 100 nm and 4 to 8 μm filters	2.5 to 3.8 μm (long wavelength required for thermal correction)	2.5 to 5 μm	1 – 5 μm	2.5 – 5 μm	10 - 30 μm	10 - 30 μm
Spectral Resolution	N/A	Narrowband	Narrowband	N/A	R~1000	R~500 (spectroscopy) R~30 (narrowband imaging)	R~300 (spectroscopy) Or R~10 narrowband filters if multispectral	dλ ~ 20 nm or better	R ~ 15,000 – 30,000	R > 5,000	R ~ 50	R ~ 50
1D, 2D, or multi-object spectroscopy?	N/A	N/A	IFU or hyperspectral imaging desirable for Jupiter and Saturn to get spatially resolved spectra at various locations across the disk	N/A	Imaging spectroscopy over Io disk; ~1.5" diameter; tens of arcseconds over Venus disk.	N/A	N/A	N/A	1D, could include/ extend to cross-dispersal of echelle orders, with consecutive orders displaced spatially from each other on the array through use of a lower resolution grating oriented perpendicular to the echelle	1D, could include/ extend to cross-dispersal of echelle orders, with consecutive orders displaced spatially from each other on the array through use of a lower resolution grating oriented perpendicular to the echelle	2D spectroscopy preferred but can be accomplished with 1D spectroscopy	1D spectroscopy required; 2D spectroscopy useful for interpretting data becasue of strong temperature variations
Spatial Resolution	Diffraction limited at 500 nm (FWHM~0.12"); high-strehl PSF (~λ/20 WFE budget)	~ 200 km/pix	Diffraction limited	Space weathering: FWHM<1" Structural changes: Diffraction limited at 500 nm (FWHM~0.12"); high-strehl PSF (~λ/20 WFE budget)	Critically-sampled UV GHAPS PSF	Diffraction limited; ~12 resolution pixels at 3.4 μm (~1 arcsec)	0.75 arcsec (1.4 km)	1 arcsec	Diffraction limited	Diffraction limited	Diffraction limited; ~ 5 - 20 km	Diffraction limited; Hemispheric / gloabal
Guiding / Pointing Performance	Jitter < ~30 mas RMS; high non-sidereal guiding rate (for NEOs, >2 degrees/day minimum)	Jitter ~30 mas RMS	Jitter ~30 mas RMS	Structural changes: Jitter < ~30 mas RMS; high non-sidereal guiding rate (for Apophis-like flyby, >40 degrees/hour)	Jitter ~30 mas RMS	~0.5 arcsec	~0.5 arcsec	Jitter: < 0.1 arcsec during a single integration Drift: < 0.1 arcsec during a single integration	Sub-arcsecond	Sub-arcsecond	Drift: < 2.5 arcsec during a single integration	Drift: < 2.5 arcsec during a single integration
Sensitivity/Associated SNR	N/A	SNR ~ 100 for visual surface brightness of ~1 magnitudes / arcsecond^2	SNR ~ 5-100 for visual surface brightness of ~10 magnitudes /	Structural changes: SNR~10 for surface brightness ~5 magnitudes /	SNR ~10 per spectral element at 1E-17 W/ m^2/A	> 15	> 100	SNR ~ 100 at V = 14	~10-19 – 10-17 W m-2 *	~10-19 W m-2 *	SNR > 100	SNR > 100
Cadence/Duty Cycle/ Total Experiment Duration	KBOs: Cadence: 1/ day - 1/quarter. Duty cycle: N/A. Duration: years NEOs: Cadence: Minutes. Duty cycle: N/A Duration: hours	texp ~ 5 sec; multiwavelength images taken every 30 minutes for total duration of ~ 4 days	texp ~ 5-30 sec depending on target; multiwavelength images taken every 10-20 minutes for total duration of ~ 4 days	Structural changes: 100 ms cadence, ~50% duty cycle, Total experiment duration of ~hours	Revisits on 2-3 hour timescale for several days to sample range of sub-observer latitudes.	Minutes to hours	0.05 s to 10 s exposures on a daily basis for a lunation or preferably longer	Measurement Dependent	Total time on source: Minutes to hours (depending on cometary activity)	Total time on source: Minutes to hours (depending on cometary activity)	< 1 min integration time per target	< 1 min integration time per target
Subsystem Temperatures	N/A	N/A	N/A	N/A	N/A.	No warmer than the telescope temperature	Cooler than the telescope temperature to not be background limiting	OTA: < 230K Detector: Instr. specific	Detector 30 K / OTA < 240 K	Detector at 30 K / OTA < 240 K	Ambient	Ambient
Footnotes					See Tsang et al. 2013 for COS observations this is modeled on.				Sensitivity is 10σ in 1 hr. Detector read noise could become substantial below 3 μm.	Sensitivity is 10σ in 1 hr. Detector read noise could become substantial below 3 μm.		1An R = 50 is sufficient to resolve oxides on the Lunar surface so it is assumed that similar oxides on Mercury will be resolvable at an R = 50 (Figure 14).

Appendix 2: UV-VIS SNR Estimation

The signal-to-noise ratio calculation in UV and visible wavelengths has two parts: calculating the signal received from the source in an exposure and calculating the noise due to all of the significant noise sources. In UV and visible wavelengths, there are four significant noise sources: Poisson shot noise from the sky background, the source itself and dark current, plus read noise of the detector. Thermal emission from the telescope optics is not considered. This is given in the equation below:

$$SNR = \frac{SRC}{\sqrt{\sigma_{SRC}^2 + \sigma_{SKY}^2 + \sigma_{DC}^2 + \sigma_{RN}^2}}$$

where *SRC* is number of photons received from the source and σ_{SRC}, σ_{SKY}, and σ_{DC} are the errors associated with counts from the source, the sky background and the dark current, respectively, and σ_{RN} is the error due to read noise. The combined noise due to all of the separate noise sources is the quadratic sum of the standard deviations (or the sum of the variances).

The standard deviation of a Poisson-distributed random variable is the square root of that variable. For example, if the average number of photons expected from the sky background during an exposure is 100, the error (standard deviation) over a sequence of exposures will be 10 photons. The same Poisson statistics apply if one considers electrons instead of photons, but it is important to be consistent (i.e., compare source counts in electrons to noise terms in electrons). In the following worked example, the conversion factor between photons and electrons is the detector quantum efficiency.

A2.1. Example SNR Calculation

Consider an exposure of a star with the GHAPS 1-m telescope. In this example, we will assume a detector with characteristics similar to the Zyla 4.2+ sCMOS camera from Andor Technologies[1]. We will also assume that there is an optical train that extends the 14 m focal length of the GHAPS telescope to 40 m in order to match the plate scale to the width of the PSF.

Table A2.1 Telescope and Detector Parameters for the SNR Worked Example

Telescope	1-m aperture, 40-m focal length, 50% end-to-end transmission
Detector	sCMOS array; 6.5 μm pitch; 82% QE, 1 e- read noise; 0.14 e-/pixel/sec dark current

[1] http://www.andor.com/pdfs/specifications/Andor_Zyla_5.5_and_4.2_PLUS_Specifications.pdf

Filter	Johnson V filter; centered at 0.55 mm, width of 0.089 μm

In a V filter, a 0-mag object has a flux of 3.64 x 10^{-9} erg cm^{-2} s^{-1} $Å^{-1}$ (Zombeck 1990). We will assume a V-band sky brightness of 21.5 magnitudes per square arcsecond (Leinert et al. 1998; Giavalisco et al. 2002). Sky brightness on a balloon depends mainly on the zodiacal background and whether the wavelength window includes OH emission lines.

Platescale:
The platescale (radians per unit length) of a telescope is 1/*FL*, where *FL* is the focal length. Since there are 206265 arcseconds per radian, the platescale of a 40-m imaging system (in arcseconds per μm) is 206265/(40 x 10^6 μm) = 0.0052"/μm. Given a pixel size of 6.5 μm, the platescale is 0.033"/pixel.

The platescale determines how many pixels need to be read to account for most of the source flux. If we use the first minimum of the Airy disk as a convenient proxy for the size of the source, then about 50 pixels lie within that minimum. $R_{min} = 1.22 \lambda/D$. Here R_{min} is the radius of the first Airy minimum, λ is wavelength and D is the telescope aperture. At λ = 0.5 μm and D = 1 m, R_{min} = 0.12", or about 4 pixels.

A2.1.1. Calculating Source Counts

Consider observations of a V=15 source from the 1-m GHAPS telescope. How many photons will be observed in a 1 second exposure?

The telescope aperture (in sq. cm) is π 50^2 = 7854 cm^2. If we include the throughput (assumed to be 50%), then the effective aperture is 3927 cm^2.

A Johnson V filter has a width of 0.089 μm or 890 Å.

A 1-sec exposure of a zero-mag star with an effective aperture of 3927 cm^2 therefore collects 890 Å x 3927 cm^2 x 1 s x 3.64 x 10^{-9} erg cm^{-2} s^{-1} $Å^{-1}$ = 0.0127 erg. A V=15 star will be 10^6 times fainter, or 1.27 x 10^{-8} erg.

To convert erg to photon, recall that the energy of a photon is hc/λ, where h = 6.626 x 10^{-27} erg/s (Planck constant), c = 2.9979 x 10^{10} cm/s (speed of light) and λ = 0.5 μm or 0.00005 cm. The number of photons per erg (at λ = 0.5 μm) is 2.52 x 10^{11}.

The number of photons from a M_v=15 star in a V filter is about 3200 photons/s. Given a QE of 82%, the number of electrons is 2624 photons/s.

A2.1.2. Calculating Noise Terms

The noise from source photons is σ_{SRC} = $2624^{.5}$ = 51.2.The photon flux from the sky is 21.5 mag/arcsec^2. The area of the circle within the first Airy minimum is about π 0.12^2 = 0.045 arcsec^2. The flux from the sky is about 0.36 photons/s or 0.30 electrons/s. The noise from sky photons is σ_{SKY} = 0.54.

Dark current will be 0.14 e^-/pixel/sec, or 7 electrons over the 50-pixel region of the Airy disk, which means that σ_{DC} = 2.65.

The read noise is assumed to be an electron per read. The read noise from a 50-pixel region is σ_{RN} = 7.1 e-.

The quadratic sum of all of the standard deviations is sqrt (51.2^2 + 0.54^2 + 2.65^2 + 7.1^2) = 51.7. The dominant noise term is the photon shot noise from the source itself.

The signal-to-noise ratio is therefore 2624/51.7 = 50.7.

A2.2. Advantages of a Balloon Platform in the UV/Optical

Balloon-borne telescopes have certain shortcomings that spacecraft do not: daytime observations suffer from high levels of scattered sunlight in UV and visible wavelengths, and balloon gondolas are subject to more severe pointing and thermal control challenges than spacecraft. Nevertheless, balloon-borne telescopes operating near 35 km have four important advantages over ground-based facilities: 1) the potential for diffraction-limited imaging, 2) access to UV wavelengths that are blocked by the Earth's atmosphere, 3) very stable photometry, and 4) very low sky backgrounds. These are each discussed in more detail below.

A2.2.1. High Acuity Imaging

One of the main advantages of balloon-borne telescopes is their freedom from seeing-induced image degradation. Ground-based telescopes with wavefront correction can compensate for seeing, but Strehl ratios for ground-based adaptive optics (AO) systems are generally better in J-H-K bands than at wavelengths shorter than 1 μm.

The Fried parameter, r_o, is a measure of the turbulence scale. For a high-quality ground-based site (e.g., the Mauna Kea Observatories), r_o is around 22 cm. For a telescope at balloon altitudes (near 35 km, above 99.5% of the Earth's atmosphere), the Fried parameter is estimated to be 250 m, based on scintillation measurements made from the MIR spacecraft of stars that were observed through the Earth's atmosphere (Ford et al. 2002). This implies that a 1 m balloon-borne telescope like GHAPS should be able to provide diffraction-limited imaging, provided that non-seeing issues such as pointing stability and optical alignment are addressed.

(ref:http://www2.keck.hawaii.edu/optics/ScienceCase/TechSciInstrmnts/Products_SeeingVarMaunaKea.pdf.)

At present, only HST surpasses the diffraction limit of a 1 m telescope (which is 0.12" at 0.5 μm). The need for such a capability is made clear by the number of awarded observing programs that use HST primarily for its spatial resolution in UV and visible wavelengths – in HST cycle 19, for example, these programs represented about a third of the total HST observing programs.

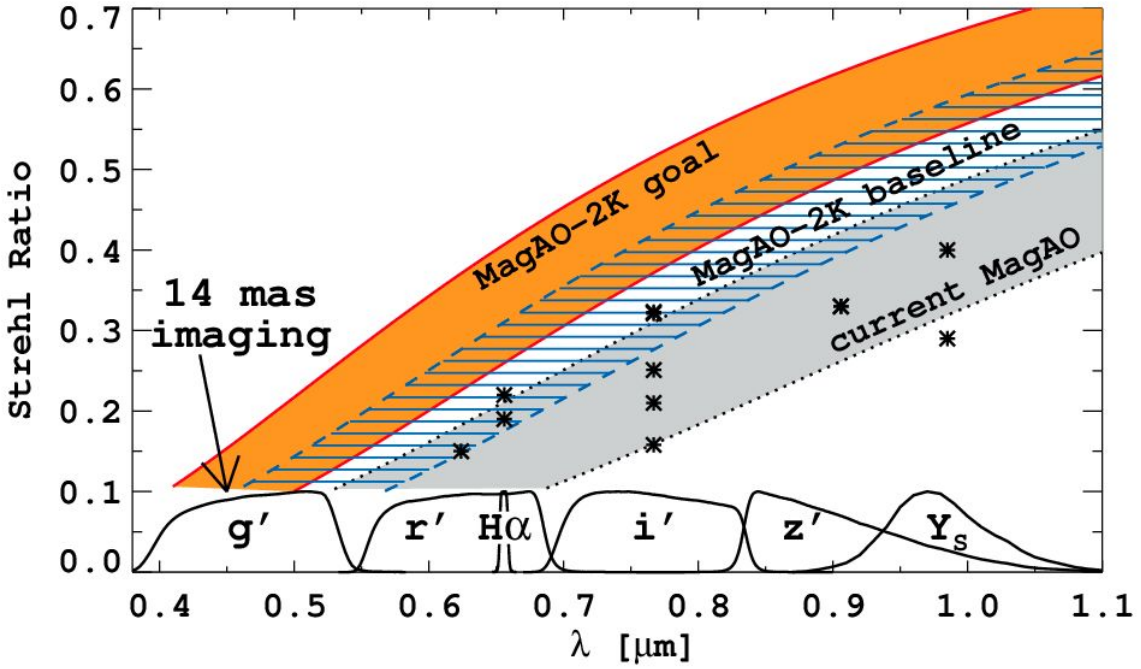

Figure A2.1. Measured Strehl ratios from the MagAO system at the Magellan telescope as a function of wavelength and predicted performance for the upcoming MagAO-2K system, which has higher cadence wavefront sensing. Credit: Males et al. (2016).

Compensating for atmospheric turbulence with adaptive optics becomes dramatically harder at shorter wavelengths. At some wavelengths, ground-based systems with state-of-the-art AO will outperform a 1 m balloon: this cross-over wavelength appears to be between 0.7 and 0.9 μm -- it depends, in part, on the application. For science cases that map the structure of extended objects, like high-acuity maps of clouds on Jupiter, a Strehl ratio of 30% might be acceptable. For other cases, like the detection of faint companions near a bright primary, a 30% Strehl ratio might contain too much light in the broad halo of the PSF.

In any case, a balloon-borne imaging system has some fundamental differences from current visible-wavelength AO systems. Unlike ground-based systems, the balloon does not need a guide source (either natural or laser guide star) – all fields are available to the balloon-borne telescope with its intrinsic PSF. In addition, the balloon should not suffer from variable seeing conditions: performance should be consistent, and therefore

amenable to post-processing, similar to HST images that use TinyTim-based synthetic PSFs for deconvolution. Finally, Fig. A2.1 shows that ground-based AO systems are not expected to perform well at 0.55 μm (the peak of the Sun's blackbody curve) or at shorter wavelengths (which may be useful for detection of haze or certain spectral features). In the wavelength regime that is shorter than 0.55 μm, a balloon-borne telescope will enable high spatial resolution science that only HST can currently address.

A2.2.2. Photometric Stability and Low Sky Background

Two factors that plague ground-based photometry are variable extinction and scintillation. Both are greatly reduced on a balloon platform. Robert et al. (2008) developed a model for scintillation from a stratospheric balloon. They show that scintillation is a concern at elevation angles very close to zero but drops very quickly at reasonable elevations (> 5°), thus scintillation noise will be less than photon shot noise due to the sky background.

The nighttime sky background can be low from balloon platforms, even though the nominal 35 km (115,000 ft) float altitude is still below many sky emission lines (particularly OH lines in the J-H-K bands). Like HST, a balloon will suffer from zodiacal light. However, a balloon-borne telescope should benefit from sky backgrounds that are equivalent to the darkest terrestrial sites.

In addition, point source observations benefit from the narrow PSFs that balloon-borne telescopes can provide. The median seeing achieved from the Canada-France-Hawaii Telescope (after dome venting) on Mauna Kea is 0.61" (Simons 2015). Therefore, if the balloon-borne PSF is less than 0.2", compared to 0.6" that one might achieve from a good ground-based site, then the background counts are reduced by a factor of nine when one adds up the pixels that include the source. To take advantage of the narrow PSF, an imaging array will need a plate scale that is commensurate with the width of the PSF.

Appendix 3: Calculating the Nominal Sensitivity of a Hypothetical GHAPS IR Science Instrument

A3.1. Sensitivity to line and continuum flux

The following sections establish the framework for predicting the expected limiting IR sensitivities of the GHAPS platform under the assumption described in § 3. We use a conventional methodology, based largely on photon counting and Poisson statistics, to estimate the noise contribution from key source mechanisms, such as the Earth's atmosphere, the primary (PM) and secondary (SM) mirrors and possible detectors used for IR spectroscopy.

GHAPS will have an outer barrel baffle, PM cone baffle in center of PM, SM cone baffle around SM to avoid unwanted stray light. These components are efficient thermal radiators that introduced undesired noise to the IR instrument, thus decreasing sensitivity, however we have neglected these sources of noise under the assumption that a proper design of a cold stop in the IR science instrument shall mask most of the emission from baffles, struts and spiders.

Our signal-to-noise ratio (SNR) estimates rely on a simple Poisson calculator that tracks read noise, collected sky flux, and collected thermal flux resulting from sky brightness, using a line-by-line radiative transfer model (Clough et al. 2005) in combination with spectral distribution of near-infrared zenith airglow measurements below 2.4 μm performed from a balloon at 30 km altitude during flights in 1972 and 1974 (at low resolution; Leinert et al. 1998 and refs. therein) and integrating the Planck function across all wavelengths at expected telescope temperature. No attempt is made to consider the serious spectroscopic case here where the airglow lines are resolved from most of the continuum making the sky background minimal. The Meinel OH bands that are the primary contributor of airglow in the 1.0 – 2.4 μm range are also prominent from 2.5 – 3.7 μm but, due to the dominance of thermal emission in this regime, have been poorly characterized. Overall, these estimates of airglow are valid for broadband observations, and we opt to neglect airglow contribution beyond 2.5 μm since either thermal background from the OTA will dominate or in case of calculations involving higher resolving power.

The calculations focus on point source limiting fluxes with extraction aperture size set by the diffraction limit of the telescope at all wavelengths from 1 – 5 μm. Estimates are based on typical integration time on source and account for nodding/background subtraction presuming the target is nodded on chip (so that the main penalty is sqrt(2) for differencing). Inefficiencies for nodding/dithering and for inefficient fast exposure times (i.e. 50 milliseconds) required for mid-IR imagery are folded into the estimates. These values are meant to be ballpark for best-case performance. Real performance could likely be different by a few tenths of a magnitude.

For GHAPS payload sensing imagers and spectrometers that use quantum detectors (e.g., CCD's or photodiodes), we describe an approach to estimate the IR instrument sensitivity at a given SNR, telescope characteristics, and integration time using:

$$SNR = \frac{Signal}{Noise}, \quad (1)$$

with $$Noise = \sqrt{Signal + RN^2 + 2\,N_{tel}{}^2 + 2\,N_{sky}{}^2} \quad (2)$$

And assuming:

Read noise: RN = 10 e^-

Noise resulting from the telescope N_{tel} [e^-] is

$$N_{tel} = \sqrt{px_{foot}\,(L_{tel}\,\varepsilon)\,\Delta\lambda\,\eta\,thr\,QE\,t_{int}} \qquad (3)$$

where:

px_{foot} sets the diffraction limited size given by the telescope aperture and instrument pixel size for every wavelength,

$$px_{foot} = \pi\left(\frac{diff_{lim}}{\varphi_{pix}}\right)^2 \qquad (4)$$

The diffraction limit (in arcseconds) at a given wavelength is

$$diff_{lim} = 206265\ \frac{1.22\,\lambda}{D_{tel}} \qquad (5)$$

And φ_{pix} is the angle subtended by edge of a pixel, i.e. φ_{pix} = *pixel size* * *platescale*, where *pixel size* is 18 μm (assumed) and *platescale* = 206256/F#$_{tel}$/D_{tel}, using an optical system focal ratio (or F# = focal length/D_{tel}) of 14 and D_{tel} is the telescope aperture of 1 m.

L_{tel} is the telescope background emission obtained from Planck's function:

$$L_{tel} = 2 \times 10^{24}\,\frac{hc^2}{\lambda^5}\,1/(exp(\frac{hc}{10^6\lambda kT}) - 1) \quad [\text{W m}^{-2}\ \text{sr}^{-1}\ \mu\text{m}^{-1}] \qquad (6)$$

Using:

Planck's constant $h = 6.62606896 \times 10^{-34}$ *J s*
Speed of light $c = 2.99792458 \times 10^{8}$ *m/s*
Boltzmann's constant $k = 1.3806505 \times 10^{-23}$ *J/K*

The mirror emissivity ε depends on its coating and the polarisation of the radiation. For instance, protected gold has ε = 2% in the 0.7 to 5 μm spectral range for non-polarized radiation. Below 0.7 μm the emissivity rapidly increases. Aluminum has ε = 7% to 10% between 0.4 to 0.7 μm spectral range. We assume 5% for the 0.7 to 5 μm spectral range, see Figure A3.1.

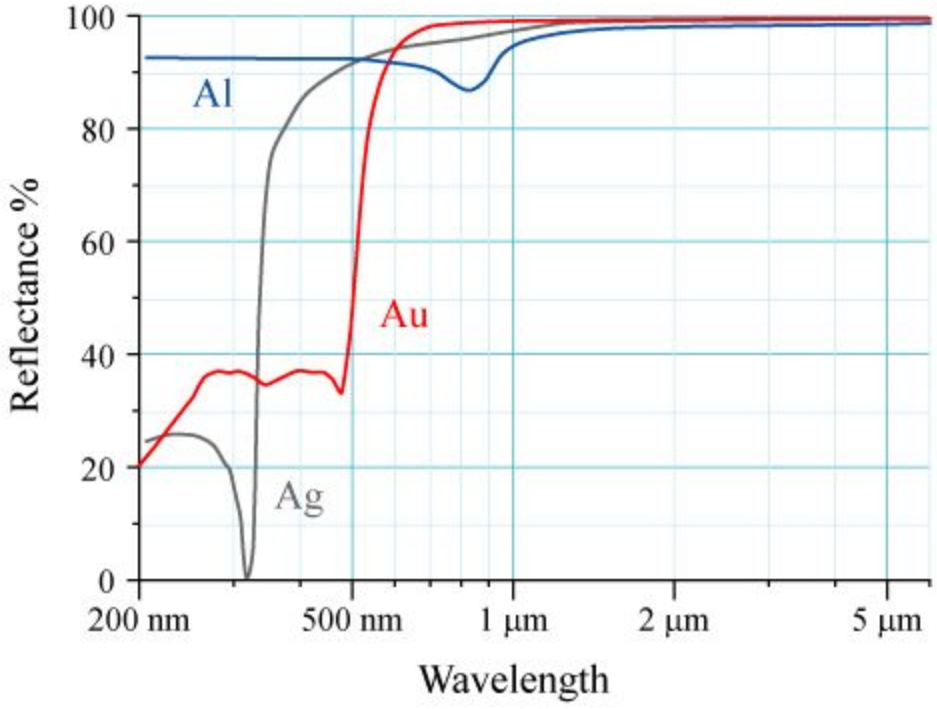

Figure A3.1. Reflectance vs wavelength curves of some common metallic vacuum evaporated coatings for mirrors at normal incidence.
https://en.wikipedia.org/wiki/Optical_coating

$\Delta\lambda=\lambda_2-\lambda_1$ is the difference between upper and lower band edges of filter. We use $\Delta\lambda = \lambda/R$, with R representing the instrument resolution.
λ is the spectral wavelength.
η is the étendue (or "A-Omega product," m^2 $arcsecond^2$) or throughput of the optical imaging system: $\eta = 1/4\pi\, D_{tel}^{\,2}\, \Phi_{pix}^{\,2}$.
thr is the system throughput (assumption: 50%).
QE is the detector quantum efficiency (assumption: 85%).
t_{int} is the total integration time on source (s).

And, **noise resulting from sky background [e^-]:**

$$N_{sky} = \sqrt{px_{foot}\, L_{sky}\, \Delta\lambda\, \eta\, thr\, QE\, t_{int}} \qquad (7)$$

where L_{sky} is obtained from LBLRTM in units of W m^{-2} sr^{-1} μm^{-1} at 36 km altitude.

Based on Eq. (1), a detected signal [e^-] at a certain detector can be obtained using:

$$D_{signal} = (SNR^2 + \sqrt{SNR^4 + 4\, SNR^2\, Noise^2})/2 \qquad (8)$$

Thus, after the total *Noise and* D_{signal} are obtained, we can estimate the sensitivity for continuum flux ($Sens_{cont}$) and line flux ($Sens_{line}$) from an unresolved point source as:

$$Sens_{cont} = D_{signal}/(t_{int}\, A_{tel}\, thr\, QE\, \Delta\lambda) \quad [\text{ph s}^{-1}\ \text{m}^{-2}\ \mu\text{m}^{-1}] \qquad (9)$$

$$Sens_{line} = D_{signal}/(t_{int}\, A_{tel}\, thr\, QE) \quad [\text{ph s}^{-1}\ \text{m}^{-2}] \qquad (10)$$

where A_{tel} is the area of the primary mirror.

Our results are shown in Fig. A3.2, and we compare GHAPS performance with airborne, ground-based and space-based IR facilities, namely SOFIA, VLT, Keck, Gemini, Spitzer, and JWST.

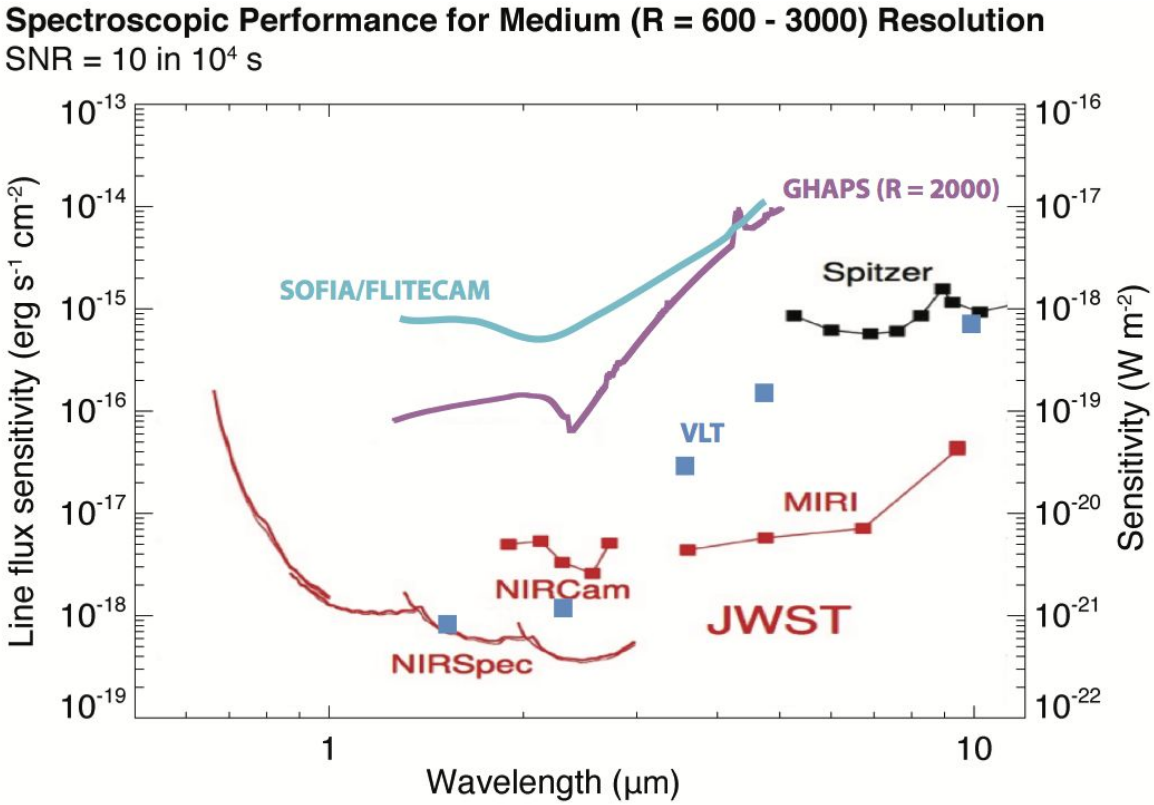

Figure A3.2. Comparison of sensitivity from a hypothetical IR spectrograph (R = 2000) onboard GHAPS vs. airborne (SOFIA), ground-based (VLT), and space-based (Spitzer, JWST) IR facilities. Sensitivity is estimated for emission line flux from an unresolved point source in an exposure time of 10^4 s. Estimates for GHAPS sensitivity consider airglow emission at wavelengths below 2.4 μm using values from Leinert et al. (1998). SOFIA/FLITECAM values are obtained from Gehrz et al. (2011), scaled by a factor of ~3 to account for an integration time of 10^4 s. Light blue squares show independent estimates for a notional instrument at VLT.
Based on: https://jwst.stsci.edu/science-planning/performance--simulation-tools-1/sensitivity-overview

A3.2. Magnitude limits

To estimate practical magnitude limits in the 3-5 μm range, we computed the signal to noise ration (SNR) under the following assumptions: an F/14 telescope with a 1-m aperture and an effective emissivity of 10% and end-to-end transmission of 50%. The spectral resolution is R = 300. The detector is modeled on an H2RG array, with 18 μm pixels, a read noise of 10 e^-, a quantum efficiency of 85% and a full well depth of 200,000 e^-.

Tables A3.2–6 show the magnitude limits at five specific wavelength bands, centered at 2.70, 3.40, 3.70, 4.27 and 4.80 μm. The rows of green text in these tables designate the transition where sky background is higher than the telescope thermal contribution. Sensitivity limits for continuum flux are taken from equation 9 in §A3.1, and converted to magnitude limits using reference values for zero magnitude flux densities from Table A3.1. The integration time for each individual exposure is 100 s, with 30 co-added exposures (3000 s of total integration time). The magnitude limit represents the brightness of an object that has an SNR of 10 per spectral band at R = 300. This spectral region is *the most sensitive* to OTA (accounting for primary and secondary mirrors only) temperature because the telescope emission scales exponentially with temperature over this range. At shorter wavelengths (e.g. 1 – 2.4 μm) the sky airglow dominates over the OTA thermal emission; at longer wavelengths (near or longward of the OTA's black body peak) the thermal emission is only a linear function of the OTA temperature. The *sky noise* is obtained from equation (7) and *OTA noise* is obtained from equation (3). These Tables highlight the impact of OTA temperature on the sensitivity of GHAPS in the 3-5 μm region. The difference in limiting magnitudes between an OTA at 300 K (the daytime/evening temperature of the BOPPS telescope) and one at 195 K are 3.4, 3.7 and 2.9 mags at λ = 3.4, 3.8 and 4.8 μm, respectively. The colder optics allow observations of objects that are a factor of more than 20 fainter, hence the OTA temperatures should be lowered as much as possible.

Table A3.1. Reference values for zero magnitude flux density.

Wavelength (μm)	1.25	1.65	2.2	2.7	3.4	4.37	4.27	4.8
Flux (Jy)[1]	1566.4	1017.8	645.0	454.0	299.5	255.0	196.7	157.5

[1] Source: https://www.gemini.edu/?q=node/11119

Table A3.2. Magnitude Limits vs. OTA Temperature at λ = 2.70 μm.

OTA Temp. (K)	**Sky Noise (e^-)**	**OTA Noise (e^-)**	**Mag. Limit (Vega)**
300	2.93E+02	2.65E+03	14.45

265	2.93E+02	8.19E+02	15.66
230	2.93E+02	1.77E+02	16.66
195	2.93E+02	2.22E+01	16.82
160[1]	2.93E+02	1.11E+00	16.83

[1] An OTA temperature of 160 K may not be realistic in practice, since severe condensation is expected to occur on the OTA surfaces.

Table A3.3. Magnitude Limits vs. OTA Temperature at λ = 3.40 µm.

OTA Temp. (K)	Sky Noise (e^-)	OTA Noise (e^-)	Mag. Limit (Vega)
300	4.08E+02	1.47E+04	12.13
265	4.08E+02	5.79E+03	13.14
230	4.08E+02	1.72E+03	14.43
195	4.08E+02	3.29E+02	15.74
160[1]	4.08E+02	3.07E+01	16.00

[1] An OTA temperature of 160 K may not be realistic in practice, since severe condensation is expected to occur on the OTA surfaces.

Table A3.4. Magnitude Limits vs. OTA Temperature at λ = 3.70 µm

OTA Temp. (K)	Sky Noise (e^-)	OTA Noise (e^-)	Mag. Limit (Vega)
300	1.33E+02	2.450+04	11.40
265	1.33E+02	1.06E+04	13.14
230	1.33E+02	3.47E+03	13.54
195	1.33E+02	7.60E+02	15.17
160[1]	1.33E+02	8.59E+01	16.79

[1] An OTA temperature of 160 K may not be realistic in practice, since severe condensation is expected to occur on the OTA surfaces.

Table A3.5. Magnitude Limits vs. OTA Temperature at λ = 4.27 µm

OTA Temp. (K)	Sky Noise (e^-)	OTA Noise (e^-)	Mag. Limit (Vega)
300	2.99E+04	5.52E+04	10.11
265	2.99E+04	2.63E+04	10.61

230	2.99E+04	9.99E+03	10.86
195	2.99E+04	2.68E+03	10.91
160[1]	2.99E+04	4.05E+02	10.92

[1] An OTA temperature of 160 K may not be realistic in practice, since severe condensation is expected to occur on the OTA surfaces.

Table A3.6. Magnitude Limits vs. OTA Temperature at λ = 4.80 µm

OTA Temp. (K)	Sky Noise (e^-)	OTA Noise (e^-)	Mag. Limit (Vega)
300	1.18E+04	9.68E+04	9.40
265	1.18E+04	5.00E+04	10.09
230	1.18E+04	2.11E+04	10.91
195	1.18E+04	6.57E+03	11.54
160[1]	1.18E+04	1.22E+03	11.68

[1] An OTA temperature of 160 K may not be realistic in practice, since severe condensation is expected to occur on the OTA surfaces.

Table A.3.7 contains estimates of the infrared performance of the GHAPS platform under the assumption that the aperture size is 1 m and that the telescope is passively cooled to 230 K. At the shortest wavelengths, 1.0-2.2 µm, thermal emission from the telescope structure and sky is largely negligible and airglow dominates the noise model. Beyond 2.2 µm thermal emission from the telescope mirrors (and to a lesser extent the (night) sky) dominates the noise. This document does not address daytime observing. These estimates rely on a simple Poisson calculator that tracks read noise, collected sky flux, and collected thermal flux using typical airglow dominated sky brightnesses in mag/arcsec^2 and integrating the Planck function across classical J, H, K, L, L', M, N, and Q bandpasses at the telescope temperature.

The cases examined in Table A.3.7 cover a range of spectral resolutions: R=10 (broadband imaging), 300 (low resolution spectroscopy), 10,000 (moderate resolution) spectroscopy, and 50,000 (high resolution spectroscopy). To understand the impact of using a system compromised by UV-Vis requirements and a higher than necessary OTA temperature, the low resolution (broadband imaging) model is evaluated for three additional situation: telescope temperature of 190 K with baseline emissivity of 10%; telescope temperature of 230 K with system emissivity of 3%; and telescope temperature of 190 K and system emissivity of 3% (representing the fully IR optimized configuration). **L- and M-band sensitivities are about 2.0-2.5 magnitudes better for this IR optimized case.**

Table A3.7. 10-sigma Vega (point source) magnitude limits for 3600 s integration time, assuming a diffraction limited image, for a variety of instrument spectral resolutions and OTA temperatures. Cells with red text are read noise limited (a read noise of 10 e^- was used for these estimates). Cells with green text have noise dominated by airglow Poisson noise.

			1.25	1.6	2.2	3.4	3.7	4.8	10.2	20	microns
R*	T**	E***	J	H	K	L	L'	M	N	Q	band
10	300	0.1	21.1	19.6	18.5	14.1	13.5	10.3	6.4	4.1	
10	230	0.1	21.1	19.6	18.9	16.2	15.5	12.5	7.7	5.0	Baseline
10	190	0.1	21.1	19.6	18.9	17.5	17.3	14.0	8.4	5.4	
10	230	0.03	21.1	19.6	18.9	16.8	16.1	13.6	8.8	6.0	
10	190	0.03	21.1	19.6	18.9	18.0	17.8	15.0	9.5	6.4	IR Optimized
300	230	0.1	18.8	17.6	16.9	14.4	13.6	11.0	6.2	3.5	
10000	230	0.1	14.5	13.8	13.0	11.5	11.0	8.7	3.9	1.2	[1]
50000	230	0.1	12.8	12.1	11.3	10.0	9.7	7.8	3.0	0.3	
IRTF R10, 280K, E=0.1			21.9	20.6	20.0	16.7	16.1	13.7	9.6	7.0	[2]
Keck R10, 280K, E=0.1			25.4	24.1	23.2	19.2	18.5	16.3	12.2	9.8	[3]

* Spectral Resolution (λ\Δλ)
** Temperature (K)
*** Emissivity
[1] instrument transmission drops from 0.5 to 0.2 for hi-res spectroscopy
[2] diffraction limited beyond K-band; 0.5" for JHK
[3] all diffraction limited

Appendix 4: Acronym List

AO	Adaptive Optics
AU	Astronomical Unit
BOPPS	Balloon Observation Platform for Planetary Science
BRRISON	Balloon Rapid Response for ISON
CCD	Charge-Coupled Device
CCKBO	Cold Classical Kuiper Belt Object
CFEPS	Canada France Ecliptic Plane Survey
CFHT	Canada-France-Hawaii Telescope
CMOS	Complementary Metal-Oxide-Semiconductor
COS	Cosmic Origins Spectrograph
FORCAST	Faint Object infraRed CAmera for the SOFIA Telescope
FOV	Field of View
FWHM	Full Width at Half Maximum
GHAPS	Gondola for High Altitude Planetary Science
HST	Hubble Space Telescope
IFU	Integral Field Unit
IR	Infrared
IRTF	Infrared Telescope Facility
ISRU	In Situ Resource Utilization
JAXA	Japanese Aerospace Exploration Agency
JWST	James Webb Space Telescope
KAO	Kuiper Airborne Observatory
KBO	Kuiper Belt Object
LWIR	Long Wave Infrared
MERTIS	Mercury Radiometer and Thermal Infrared Spectrometer
MODTRAN	MODerate resolution atmospheric TRANsmission
MWIR	Mid Wave Infrared
NASA	National Aeronautics and Space Administration
NEA	Near Earth Asteroid
NEO	Near Earth Object
NIR	Near Infrared
NIRSpec	Near InfraRed Spectrograph
NUV	Near Ultraviolet
OD	Optical Density
OMCT	Oxygen-Metal Charge Transfer
OPIS	Observatory for Planetary Investigations from the Stratosphere
OSSOS	Outer Solar System Origins Survey
OTA	Optical Telescope Assembly
PSF	Point Spread Function
PSNIT	Point Source Normalized Irradiance Transmittance
RMS	Root Mean Square
SIDT	Science Instrument Definition Team
SNR	Signal-to-Noise Ratio

SOFIA	Stratospheric Observatory for Infrared Astronomy
TIR	Thermal Infrared
UV	Ultra Violet
VLT	Very Large Telescope
WASP	Wallops ArcSecond Pointing
WCS	World Coordinate System
WFE	Wave Front Error